Obtaining vector magnetic field maps from single-component measurements of geological samples

Eduardo A. Lima[1] and Benjamin P. Weiss[1]

[1] Maxwell's equations can be used to demonstrate that the components of a static magnetic field in a region of space devoid of sources are not independent. This means that magnetometers that measure a single component of the magnetic field can potentially obtain all of three components of the field external to a source. Here we present an improved technique in the Fourier domain which can obtain the complete vector field planar map from just the planar map of one component. This technique is fast, robust, does not rely on any specific source type or configuration, and does not require the formulation of an inverse problem. An in-depth analysis of the advantages and shortcomings of the technique is presented, demonstrating that high-quality three-component field maps with virtually no information loss can be obtained when proper sensor and mapping configurations are used. Several results derived from both synthetic and experimental data are presented. In particular, practical cases are shown where vector maps can assist the analysis of magnetic properties of geological samples. MATLAB® routines implementing the basic vector map calculation algorithm are available as auxiliary materials and can be readily adapted for processing magnetic data obtained from a variety of magnetic sensors.

1. Introduction

[2] Magnetic studies of earth and planetary materials can greatly benefit from an understanding of magnetization at fine spatial scales. Scanning magnetometry is a powerful tool for this purpose, because it can map inhomogenous magnetization at submillimeter scales. Since both the magnetic field and magnetization are vector quantities, the ideal scanning magnetometer would measure all three orthogonal components of the field above the sample. However, owing to technical difficulties, most high-resolution scanning magnetometers measure a single component of the magnetic field. For instance, nearly all superconducting quantum interference device (SQUID) microscopes measure solely the vertical component [*Weiss et al.*, 2007].

[3] In theory, noiseless measurements of a single component of the magnetic field everywhere in an infinite horizontal plane above a sample will contain all of the information about the field everywhere in the half-space above the sample [*Lima et al.*, 2006; *Roth et al.*, 1989; *Tan et al.*, 1996]. However, a number of studies in a variety of disciplines have demonstrated that, in practice, knowledge of all three components of the field better constrain the vector magnetic field and its sources compared to just single-component data. For instance, it has recently been demonstrated that inversions of three-component biomagnetic field maps yield more accurate current distribution solutions than inversions of any individual single-component maps [*Arturi et al.*, 2004; *Bradshaw et al.*, 1999; *Di Rienzo et al.*, 2005]. Likewise, there is a growing consensus that modeling of the geomagnetic field [*Langel et al.*, 1982; *Langel and Hinze*, 1998; *Purucker*, 1990] and the use of aeromagnetic field maps for constraining crustal magnetization [*Langel et al.*, 1982] based on three-component maps yield more accurate and stable solutions than those based on total magnetic field (i.e., field strength) maps. The main reason for the practical advantage of vector data is that given that infinitely many magnetization distributions can produce a given magnetic field pattern outside the magnetized region [*Lima et al.*, 2006], having three times the number of field constraints might provide more stable, accurate magnetization inversions in the face of inevitable computational and measurement noise (see Appendix A).

[4] Direct measurement of the three components of the magnetic field is difficult in scanning magnetometry because sensors cannot be made arbitrarily small owing to physical limitations set by the small sensor-to-sample distance and because sensitivity usually scales with the size of the sensor. The space required for multiple sensors typically means that the effective sensor-to-sample distance must be larger than that of single-sensor systems, which implies that multiple-sensor systems usually have relatively lower spatial resolution and moment resolution. This is of particular concern when sensors for measuring the tangential field are to be added to vertical-component single-axis systems like

[1]Department of Earth, Atmospheric, and Planetary Sciences, Massachusetts Institute of Technology, Cambridge, Massachusetts, USA.

SQUID microscopes: the finite dimensions of tangential sensors mean that they typically require either higher effective sensor-to-sample distances compared to vertical sensors of the same size or else have smaller sizes, and possibly inferior sensitivity, in order to maintain the same distance [e.g., *Ketchen et al.*, 1997]. Additional problems arise from the fact that the sensors do not detect field components at the same position, and their relative orientation can never be made perfectly orthogonal. Similar issues take place when trying to obtain a vector field map by successively scanning each component using a single-axis sensor. In view of all these difficulties, it would be of great advantage to use single-axis magnetometers to map only one component of the field produced by a geological sample, and yet be able to obtain full vector field maps.

[5] This is a reasonable proposition because, as mentioned earlier, the three components of the static magnetic field external to a source are not independent of each other. In geomagnetism, this relationship was first investigated in the 1940s by *Vestine and Davids* [1945], and *Hughes and Pondrom* [1947], who established that the vertical and horizontal components of anomaly fields could be obtained from total field maps by means of surface integrals. With the advancement of computer technology and the development of fast Fourier transform (FFT) algorithms, *Lourenco and Morrison* [1973] proposed in the early 1970s a method in the Fourier domain to transform a map of the total field anomaly into maps of the three Cartesian components. Later, a number of groups provided derivations of Fourier relations among derivatives of both magnetic [*Pedersen*, 1989; *Pedersen et al.*, 1990] and gravity [*Hinojosa and Mickus*, 2002; *Mickus and Hinojosa*, 2001; *Nelson*, 1986, 1988] potential fields. The drawback of all of these Fourier methods is that they require knowledge of the magnetic field at all points on a surface and impose strong conditions on magnetic field spatial distribution, such as assuming the anomaly field is zero at the boundaries of the map. In addition, singularities in the equations may lead to inaccuracies in the field maps obtained under particular conditions [*Purucker*, 1990]. Hence, to overcome some of these issues, different approaches were developed, mainly in the space domain, such as convolution-based techniques [*Bhattacharyya*, 1977] and equivalent source techniques [*Galliher and Mayhew*, 1982; *Langel et al.*, 1982; *Purucker*, 1990].

[6] Because aeromagnetic surveys and analysis of satellite magnetic data have often employed total field magnetometers, the aforementioned methods aimed primarily to retrieve field component maps from total field maps. Relationships between magnetic field components in the Fourier domain have also been described for specific source types (either current distributions or magnetization distributions) and source configurations (two-dimensional distributions) [*Egli and Heller*, 2000; *Volk et al.*, 2008]. The main disadvantage of the latter approaches is that they strongly depend on assumptions regarding the sources of magnetic field. Consequently, the conditions for and the implications of the interdependency of field components have not been fully developed and exploited in the analysis of the magnetic properties of geological samples.

[7] In their original forms, all of the above techniques have limited use for scanning magnetometry and magnetic microscopy, for which one would like to use single-component

field maps to compute the two remaining components and total field map without any assumptions about the sources. Here we describe an improved technique in the Fourier domain similar to the method of *Lourenco and Morrison* [1973]. We chose to develop this in Fourier domain for two reasons. First, it is much faster and requires less computation power than space domain techniques. Second, scanning magnetometry, which involves the mapping of localized samples in near-zero magnetic field environments, very closely meets the assumption that the magnetic field is zero at the boundaries of the mapping region (which is not typically met in geomagnetic and crustal field mapping).

[8] We provide a step-by-step derivation of several relationships in the Fourier domain, directly from Maxwell's equations, which tie the three components of a static magnetic field in a source-free region of the space. In addition, we characterize the singularities in the equations in the continuous domain and establish their effect on the estimated field maps, which are independent of discretization schemes. Our analysis incorporates the requirements and peculiarities of scanning magnetometry, allowing us to ascertain what sensor and mapping configurations are best suited to obtain high-quality vector field maps in this application. We present the mathematical foundation of the technique, paying particular attention to important practical aspects of its implementation that may directly impact the quality of the estimated field maps. Specifically, we show that the major source of error is related to the size of the mapping area, and we derive formulas to quantify this error. Several examples, both with synthetic and experimental data, demonstrate the performance of the technique under different conditions. In particular, we show how the technique can be applied to magnetic field maps of geological samples measured by a SQUID microscope. A MATLAB® program (Software S1 and S2) illustrating the vector field map calculation algorithm is available as auxiliary material.[1]

2. Foundations

[9] Our goal is now to investigate whether it is possible to obtain all three components of the magnetic field from a planar map of a single component. We consider the realistic situation in which a magnetic sensor measures a single field component on a plane above a sample. Since the magnetometer detects the magnetic field external to the source, we seek to derive relationships between the three components of the magnetic field in a source-free region. These relationships should not depend on the source type or configuration.

[10] Without loss of generality, we begin by assuming that all sources are located at or below the plane $z = 0$, so that the half-space $z > 0$ is a source-free region. We also assume that the magnetic field does not change with time (magnetostatics) or that it varies sufficiently slowly such that time derivatives can be neglected. In a source-free region, the magnetic induction $\vec{B}$ is governed both by Gauss's law for magnetism

$$\nabla \cdot \vec{B} = 0, \qquad (1)$$

and by the simplified Ampère's circuital law

$$\nabla \times \vec{B} = \vec{0}. \tag{2}$$

[11]   In Cartesian coordinates, (2) corresponds to the following three equations

$$\frac{\partial B_z}{\partial y} - \frac{\partial B_y}{\partial z} = 0; \frac{\partial B_z}{\partial x} - \frac{\partial B_x}{\partial z} = 0; \frac{\partial B_x}{\partial y} - \frac{\partial B_y}{\partial x} = 0, \tag{3}$$

where z is the vertical (out of plane) coordinate and x and y are the two in-plane coordinates. Since this set of partial differential equations is valid in the domain $-\infty < x < +\infty$ and $-\infty < y < +\infty$, we can take the two-dimensional Fourier transform [*Zauderer*, 1988], yielding

$$(ik_y)b_z(k_x,k_y,z) - \frac{\partial b_y(k_x,k_y,z)}{\partial z} = 0; \tag{4}$$

$$(ik_x)b_z(k_x,k_y,z) - \frac{\partial b_x(k_x,k_y,z)}{\partial z} = 0; \tag{5}$$

$$(ik_y)b_x(k_x,k_y,z) - (ik_x)b_y(k_x,k_y,z) = 0, \tag{6}$$

where i stands for the imaginary unit, k_x and k_y are the horizontal wave numbers or spatial frequencies, and b_x, b_y, and b_z denote the Fourier transforms of B_x, B_y, and B_z, respectively. We explicitly show the dependence on space and frequency variables for clarity, and we use the following definition of the Fourier transform pair $H(x, y, z)$, $h(k_x, k_y, z)$:

$$h(k_x,k_y,z) = \int\limits_{-\infty}^{+\infty} \int\limits_{-\infty}^{+\infty} H(x,y,z)e^{-i(k_x x+k_y y)}dx\,dy; \tag{7}$$

$$H(x,y,z) = \frac{1}{(2\pi)^2} \int\limits_{-\infty}^{+\infty} \int\limits_{-\infty}^{+\infty} h(k_x,k_y,z)e^{i(k_x x+k_y y)}dk_x\,dk_y. \tag{8}$$

[12]   Notice that (6) ties the x and y components of the magnetic field via their Fourier transforms, while (4) and (5) show a more complex dependence between the transform of the z component and the z derivative of the transforms of the horizontal components. Specifically, (6) shows that by mapping one of the horizontal field components we can estimate the other component by means of simple algebraic operations performed in the spatial frequency domain, followed by an inverse transform operation. (Because some information is likely to be lost in this process, we refer to the output data of the processing as an estimated or recovered magnetic field component map. We refer to the field component map from which other components are estimated as the primary field map.)

[13]   Using the definition of the partial derivative, (4) becomes

$$\lim_{\delta z \to 0} \frac{b_y(k_x,k_y,z+\delta z) - b_y(k_x,k_y,z)}{\delta z} = (ik_y)b_z(k_x,k_y,z). \tag{9}$$

Since we are in a source-free region, we can make use of upward continuation [*Blakely*, 1996] to further simplify (9):

$$\lim_{\delta z \to 0} \frac{b_y(k_x,k_y,z)e^{-\sqrt{k_x^2+k_y^2}\,\delta z} - b_y(k_x,k_y,z)}{\delta z} = (ik_y)b_z(k_x,k_y,z). \tag{10}$$

Applying l'Hôpital's rule to evaluate the limit, we obtain

$$-k\,b_y(k_x,k_y,z) = ik_y\,b_z(k_x,k_y,z), \tag{11}$$

where $k = \sqrt{k_x^2 + k_y^2}$. Finally, rearranging (11) we get

$$b_y(k_x,k_y,z) = -(ik_y/k)b_z(k_x,k_y,z), \tag{12}$$

for $k \neq 0$. Similarly, we can derive

$$b_x(k_x,k_y,z) = -(ik_x/k)b_z(k_x,k_y,z). \tag{13}$$

These last two equations demonstrate that knowledge of the map of the vertical field component allows us to obtain both of the horizontal components. Thus, the three equations (6), (12), and (13) completely link the components of the magnetic field, establishing the interdependence between them.

[14]   Another relationship between the three components can be established by taking the two-dimensional Fourier transform of (1)

$$(ik_x)b_x(k_x,k_y,z) + (ik_y)b_y(k_x,k_y,z) + \frac{\partial b_z(k_x,k_y,z)}{\partial z} = 0. \tag{14}$$

Using the partial derivative definition and L'Hôpital's rule, and rearranging terms, we get

$$b_z(k_x,k_y,z) = (ik_x/k)b_x(k_x,k_y,z) + (ik_y/k)b_y(k_x,k_y,z). \tag{15}$$

This equation permits us to calculate the vertical field component from the two horizontal field components. Note that this equation is not independent from (6), (12), and (13). For instance, the latter can be obtained by direct substitution of (6) into (15).

3.   Singularities

3.1.   Nature of the Problem

[15]   An inspection of equations (12), (13), and (15) reveals that each break down for $k = 0$, for which there is a singularity at the origin of the spatial frequency plane. Consequently, any information associated with $k = 0$, such as the uniform component (i.e., spatial DC offset) of field maps, cannot be retrieved by these expressions. This information loss is not surprising, because both (1) and (2) are partial differential equations involving only first-order derivatives. To better understand why the three equations break down, we notice that there is a jump discontinuity [*Thomson et al.*, 2001] at the origin for the functions $k_x / \sqrt{k_x^2 + k_y^2}$ and $k_y / \sqrt{k_x^2 + k_y^2}$, which can be easily verified by observing that they assume different finite values depending on which direction the origin is

approached. This means that the limit of these functions at the origin does not exist. However, it is important to realize that these functions are bounded and do not diverge near the origin, since for any real variables u and v the following relations hold

$$\left| \frac{u}{\sqrt{u^2 + v^2}} \right| = \frac{|u|}{\sqrt{u^2 + v^2}} = \frac{\sqrt{u^2}}{\sqrt{u^2 + v^2}} \leq \frac{\sqrt{u^2 + v^2}}{\sqrt{u^2 + v^2}} = 1,$$

provided $u \neq 0$ or $v \neq 0$. (16)

Therefore, we can extend the functions so that they are defined over the whole spatial frequency plane

$$g_1(k_x, k_y) = \begin{cases} k_x / \sqrt{k_x^2 + k_y^2}, & \text{if } k_x \neq 0 \text{ or } k_y \neq 0 \\ 0, & \text{if } k_x = k_y = 0, \end{cases} \quad (17)$$

$$g_2(k_x, k_y) = \begin{cases} k_y / \sqrt{k_x^2 + k_y^2}, & \text{if } k_x \neq 0 \text{ or } k_y \neq 0 \\ 0, & \text{if } k_x = k_y = 0. \end{cases} \quad (18)$$

Even though the choice of the value of the functions at the origin is somewhat arbitrary in this case, a zero value seems to be a logical option, as it is the midpoint of the jump discontinuity and it yields a predictable null uniform component for every field map, highlighting the loss of information. In addition, because the functions g_1 and g_2 have unity extrema (as established in (16)), (12), (13) and (15) do not amplify noise in the magnetic field data, which is a very desirable feature when using real data and numerical algorithms. If we think of g_1 and g_2 as spatial filters acting on magnetic field maps, it is easy to realize that noise is filtered out, since these functions act as low-pass spatial filters. Thus, field component estimates obtained through these equations will always be less noisy than the primary field maps.

[16] Now let us turn our attention to equation (6), which breaks down in a wider range of spatial frequencies: along a line instead of at a single point. If we try to determine b_x from b_y, the equation breaks down for $k_y = 0$, while the problem manifests for $k_x = 0$ when we attempt to retrieve b_y from b_x. A similar issue is observed when rearranging (12) and (13) to retrieve b_z from the transform of one of the horizontal components. This means that any part of the field component that does not depend on one of the spatial frequency variables k_x and k_y (e.g., uniform in one direction) may not be retrieved. Moreover, the functions

$$h_1(k_x, k_y) = k_x / k_y, \quad \text{for } k_y \neq 0 \quad (19)$$

$$h_2(k_x, k_y) = k_y / k_x, \quad \text{for } k_x \neq 0 \quad (20)$$

$$h_3(k_x, k_y) = \sqrt{k_x^2 + k_y^2} / k_x, \quad \text{for } k_x \neq 0 \quad (21)$$

$$h_4(k_x, k_y) = \sqrt{k_x^2 + k_y^2} / k_y, \quad \text{for } k_y \neq 0 \quad (22)$$

tend to infinity near the singularities (i.e., they are unbounded), which indicates the occurrence of essential discontinuities [*Thomson et al.*, 2001]. Consequently, the Fourier transforms of the field components cannot be recovered in a band of frequencies around the singularities, which may result in significant information loss. Notice, however, that (15) provides a way around this problem in the particular case of estimating the z component, the trade-off being that knowledge of both x and y components is required.

[17] We can also extend the above functions so that they are defined over the whole spatial frequency plane. However, because they tend to infinity as the singularities are approached, we need to use a different scheme. We utilize the following extension

$$h_j'(k_x, k_y) = \begin{cases} h_j(k_x, k_y), & \text{if } |h_j(k_x, k_y)| \leq \gamma \\ \gamma \, \text{sgn}(h_j(k_x, k_y)), & \text{if } \gamma < |h_j(k_x, k_y)| < \infty \\ 0, & \text{at the singularities of } h_j(k_x, k_y), \end{cases}$$
(23)

where $1 \leq j \leq 4$, γ is a threshold, and sgn stands for the signum function $\text{sgn}(z) = \begin{cases} z/|z|, & \text{if } z \neq 0 \\ 0, & \text{if } z = 0 \end{cases}$. This definition limits the magnitude of the extended function to the value γ near the singularities, while preserving the phase or sign information. Particularly, there is no information loss in the region of the spatial frequency plane where $|h_j(k_x, k_y)| \leq \gamma$, because $h_j'(k_x, k_y)b_{y,x}(k_x, k_y, z) = h_j(k_x, k_y)b_{y,x}(k_x, k_y, z)$ in this region.

[18] In order to illustrate the connection between γ and noise levels, suppose the field map is corrupted by an additive noise component $N(x, y)$. The Fourier transform of the estimate is then

$$\hat{b}_{z,x,y}(k_x, k_y, z) = h_j'(k_x, k_y)b_{y,x}(k_x, k_y) + h_j'(k_x, k_y)n(k_x, k_y), \quad (24)$$

where n and b are the transforms of the noise component and noiseless field component, respectively. This demonstrates that the noise is amplified at all spatial frequencies where $|h_j'(k_x, k_y)| > 1$, and the maximum magnification factor is γ. Considering that γ also regulates the amount of distortion introduced in the recovered field (it determines the size of the region where h and h' coincide), there is a clear compromise: increasing γ improves accuracy and reduces information loss, while decreasing γ tames noise amplification. The amount of noise contamination in experimental data is what usually dictates the threshold level. Essentially, the parameter γ should be as large as possible, while avoiding excessive noise amplification. Typical values range between 100 and 100,000.

3.2. Simple Examples: Infinite Wire and Dipole

[19] In order to better illustrate the effects of the different type of singularities on the estimated field maps, we analyze two simple cases: an infinite current-carrying wire and a magnetic dipole. Because the expressions for the magnetic field produced by these sources are well known, we can

easily establish how the estimated field components differ from the actual components.

3.2.1. Infinite Wire

[20] For a wire oriented in the y direction, the three Cartesian components of the magnetic field are

$$B_x(x,y,z) = \frac{\mu_0 I}{2\pi} \frac{-z}{x^2 + z^2}; \quad B_y(x,y,z) = 0;$$
$$B_z(x,y,z) = \frac{\mu_0 I}{2\pi} \frac{x}{x^2 + z^2}, \tag{25}$$

where μ_0 is the permeability of free space and I is the current flowing through the wire.

[21] The corresponding Fourier transforms are given by

$$b_x(k_x, k_y, z) = -(\mu_0 I/2)e^{-z|k_x|}\,\delta(k_y); \tag{26}$$

$$b_y(k_x, k_y, z) = 0; \tag{27}$$

$$b_z(k_x, k_y, z) = \begin{cases} -i(\mu_0 I/2)\dfrac{k_x}{|k_x|}e^{-z|k_x|}\,\delta(k_y), & \text{if } k_x \neq 0 \\ 0, & \text{if } k_x = 0, \end{cases} \tag{28}$$

where the delta functions express mathematically the lack of dependence of the field components on the y coordinate. (The value of b_z at $k_x = 0$ is stated explicitly because otherwise the expression would not be defined at these frequencies.)

[22] We begin by noticing that the integral of B_z over the whole x-y plane is zero, because it exhibits odd symmetry. In contrast, the integral of the B_x over the same region is infinite, reflecting the fact that this component is always negative (for a positive fixed value of z) and is uniform along the y direction. These integrals correspond to the value of the Fourier transforms (28) and (26), respectively, at the origin of the spatial frequency plane.

[23] In order to illustrate the loss of the uniform part of the maps, let us estimate b_x from b_z by means of (13) and (28):

$$\hat{b}_x(k_x, k_y, z) = \begin{cases} -(\mu_0 I/2)\dfrac{|k_x|}{k}e^{-z|k_x|}\,\delta(k_y), & \text{if } k_x \neq 0 \\ 0, & \text{if } k_x = 0, \end{cases} \tag{29}$$

where the hat symbol denotes an estimate of a field component or of its transform. This expression can be further simplified by means of the following property of the delta function

$$f(u)\delta(u - u_0) = f(u_0)\delta(u - u_0), \tag{30}$$

for a function f continuous at u_0 [Bracewell, 1999].

[24] Hence, $\left(|k_x|\big/\sqrt{k_x^2 + k_y^2}\right)\delta(k_y) = \left(|k_x|\big/\sqrt{k_x^2}\right) \times \delta(k_y) = (|k_x|/|k_x|)\delta(k_y) = \delta(k_y)$, for $k_x \neq 0$, which combined with (29) results in

$$\hat{b}_x(k_x, k_y, z) = \begin{cases} -(\mu_0 I/2)e^{-z|k_x|}\,\delta(k_y), & \text{if } k_x \neq 0 \\ 0, & \text{if } k_x = 0. \end{cases} \tag{31}$$

Clearly, $\hat{b}_x$ has a zero at the origin of the frequency plane, meaning the estimated x component of the field, $\hat{B}_x$, has a zero uniform part. This is in direct contrast to (26), whose value at the origin of the frequency plane is infinite and is associated with a uniform component.

[25] Now let us consider estimating b_x and b_z from b_y by rearranging (6) and (12). In this case, it is trivial to see that such estimates are of little use, as they are both null because $b_y(k_x, k_y, z)$ is zero everywhere. In other words, meaningful estimates cannot be obtained since B_y does not vary in the y direction. This is masked in this example, however, because B_y is identically null. Hence, we turn to the field produced by a magnetic dipole to further examine this issue.

3.2.2. Dipole

[26] The three Cartesian components of the magnetic field generated by a magnetic dipole located at the origin with moment m and pointing in the z direction are

$$B_x(x,y,z) = \frac{\mu_0 m}{4\pi} \frac{3xz}{(x^2 + y^2 + z^2)^{5/2}};$$
$$B_y(x,y,z) = \frac{\mu_0 m}{4\pi} \frac{3yz}{(x^2 + y^2 + z^2)^{5/2}};$$
$$B_z(x,y,z) = \frac{\mu_0 m}{4\pi}\left[\frac{3z^2}{(x^2 + y^2 + z^2)^{5/2}} - \frac{1}{(x^2 + y^2 + z^2)^{3/2}}\right]. \tag{32}$$

[27] The corresponding Fourier transforms are given by

$$b_x(k_x, k_y, z) = -i\mu_0 m(k_x/2)e^{-zk}; \tag{33}$$

$$b_y(k_x, k_y, z) = -i\mu_0 m(k_y/2)e^{-zk}; \tag{34}$$

$$b_z(k_x, k_y, z) = \mu_0 m(k/2)e^{-zk}, \tag{35}$$

where $k = \sqrt{k_x^2 + k_y^2}$. We notice that none of the components has a uniform part, as $b_x(0, 0, z) = b_y(0, 0, z) = b_z(0, 0, z) = 0$. Moreover, (1) B_z is axisymmetric around the z axis (whence its Fourier transform depends only on k), (2) b_x is zero for $k_x = 0$, and (3) b_y is zero for $k_y = 0$. In the case of the magnetic dipole, it is straightforward to see that owing to the lack of uniform parts in the magnetic field components, the estimates $\hat{b}_x$ and $\hat{b}_y$ obtained by means of (12) and (13) correspond exactly to the transforms b_x and b_y, respectively. That is, there is no information loss in this situation.

[28] Let us now consider we wish to utilize (19)–(22) and (23) to estimate B_x from B_y, and vice versa, or to estimate the vertical component from either B_x or B_y. At first glance, one would be tempted to set aside (23) and think that there is no information loss, as there seems to be a "pole-zero cancellation" (that is, a frequency variable in the numerator canceling out a corresponding variable in the denominator). There are a number of reasons why this approach is not feasible in practice, including extremely large amplification of noise (which is present in all experimental data), numerical instability, and lack of a priori knowledge about whether a cancellation exists for an unidentified field source. These issues stem from essential discontinuities present in (19)–(22), as opposed to the jump discontinuities

observed in the expressions $k_x\big/\sqrt{k_x^2+k_y^2}$ and $k_y\big/\sqrt{k_x^2+k_y^2}$. Thus, it is necessary to employ (23) or a similar approach for handling mathematical singularities in the estimation process. However, the analysis gets more difficult owing to the introduction of nonlinear operations.

[29] The four remaining estimates are given by

$$\hat{b}_x(k_x,k_y,z)$$
$$=\begin{cases} -i\mu_0 m(k_x/2)e^{-zk}, & \text{if } |k_x/k_y| \le \gamma \\ -i\mu_0 m\,\gamma(k_y/2)e^{-zk}\,\text{sgn}(k_x/k_y), & \text{if } \gamma < |k_x/k_y| < \infty\ ; \\ 0, & \text{if } k_y = 0 \end{cases} \qquad (36)$$

$$\hat{b}_y(k_x,k_y,z)$$
$$=\begin{cases} -i\mu_0 m(k_y/2)e^{-zk}, & \text{if } |k_y/k_x| \le \gamma \\ -i\mu_0 m\,\gamma(k_x/2)e^{-zk}\,\text{sgn}(k_y/k_x), & \text{if } \gamma < |k_y/k_x| < \infty\ ; \\ 0, & \text{if } k_x = 0 \end{cases}$$
$$\qquad (37)$$

$$\hat{b}_z(k_x,k_y,z)$$
$$=\begin{cases} \mu_0 m(k/2)e^{-zk}, & \text{if } |k/k_x| \le \gamma \\ \mu_0 m\,\gamma(k_x/2)e^{-zk}\,\text{sgn}(k/k_x), & \text{if } \gamma < |k/k_x| < \infty\ ; \\ 0, & \text{if } k_x = 0 \end{cases} \qquad (38)$$

$$\hat{b}_z(k_x,k_y,z)$$
$$=\begin{cases} \mu_0 m(k/2)e^{-zk}, & \text{if } |k/k_y| \le \gamma \\ \mu_0 m\,\gamma(k_y/2)e^{-zk}\,\text{sgn}(k/k_y), & \text{if } \gamma < |k/k_y| < \infty \\ 0, & \text{if } k_y = 0. \end{cases}$$
$$\qquad (39)$$

3.3. Implications

[30] We have just shown how severe information loss is associated with essential discontinuities, while jump discontinuities only experience loss of information at $k = 0$. This indicates that the best approach for minimizing information loss consists in measuring the component perpendicular to the measurement plane and then obtaining the two remaining components via (12) and (13). It is superior in this sense to using measurements of one of the horizontal components to obtain the other horizontal component via (6) and the vertical component by rearranging (12) or (13) accordingly; measurements of both horizontal components are required to avoid the essential discontinuities when calculating the vertical component by means of (15). Owing to its unambiguously superior performance, we will focus on the vertical component mapping approach from this point forward. Our SQUID microscope system [*Fong et al.*, 2005] fortuitously incorporates this sensor/mapping configuration: the magnetic sensor is oriented along the z (vertical) direction and the field is mapped on the horizontal plane $z = h$, where h is the sample-to-sensor distance.

[31] An important point is that for most magnetic field sources, we can actually retrieve the three components of the magnetic field in practice without any significant information loss using this scheme. The rapid falloff of

magnetic fields with distance from magnetic sources guarantees that the boundaries of mapping area can be extended far enough to include regions where the total field is essentially zero, thus eliminating the ambiguity regarding the Fourier transform at $k = 0$. By forcing all components of the recovered vector field to be zero within the appropriate region, an accurate estimate of the transform at the origin of the spatial frequency plane is automatically obtained. As discussed below, extending the mapping area also improves the performance of the technique, leading to smaller error in the estimation process. Note that this procedure can be easily carried out in the case of geological samples. This is a fundamental difference between mapping of geological samples and aeromagnetic or satellite surveys of anomaly fields.

4. Experimental Constraints

[32] In the previous derivations, we assumed that the field is known everywhere in a horizontal plane. Of course, such condition cannot be met in practice, as it implies measuring an infinite amount of data. Therefore, two approaches are usually employed in real magnetic field mapping: restricting the mapping area and discretizing the field map (sampling on a grid). We next describe the effects of these limitations on the technique and how they can be minimized.

4.1. Finite Mapping Area

[33] The effects of restricting the mapping area may be analyzed by modeling the measured field as the true magnetic field in the mapping plane multiplied by a rectangular window, χ, representing the mapping area:

$$\tilde{B}_l(x,y,z) = B_l(x,y,z)\chi(x,y), \qquad (40)$$

where l stands for x, y, or z, and $\chi(x, y) = \begin{cases} 1, & \text{inside mapping area} \\ 0, & \text{otherwise.} \end{cases}$

[34] In the spatial frequency domain, (40) becomes a convolution

$$\tilde{b}_l(k_x,k_y,z) = (1/4\pi^2)b_l(k_x,k_y,z) * \text{X}(k_x,k_y)$$
$$= (1/4\pi^2) \int_{-\infty}^{+\infty}\int_{-\infty}^{+\infty} b_l(\xi,\eta)\text{X}(k_x-\xi,k_y-\eta)\,d\xi\,d\eta, \qquad (41)$$

where $*$ denotes a two-dimensional convolution operation. Now let us analyze what effects the mapping area poses on the estimated x component of the magnetic field in (13). We begin by making use of the following identity

$$B_z(x,y,z) = [\chi(x,y) + (1 - \chi(x,y))]B_z(x,y,z)$$
$$= [\chi(x,y) + \overline{\chi}(x,y)]B_z(x,y,z), \qquad (42)$$

where $\overline{\chi}(x, y) = 1 - \chi(x, y)$ is the complement of χ, that is, $\overline{\chi}$ is one everywhere but within the mapping area, where it is zero. Thus,

$$\tilde{B}_z(x,y,z) = \chi(x,y)\,B_z(x,y,z) = B_z(x,y,z) - \overline{\chi}(x,y)B_z(x,y,z). \qquad (43)$$
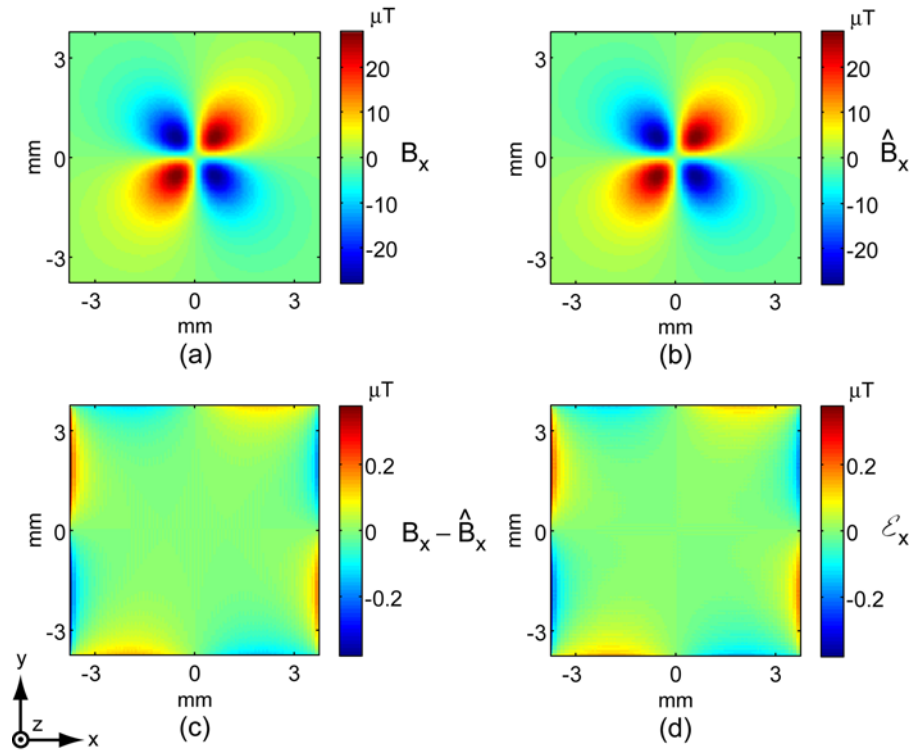
Figure 1. Results of the technique for a synthetic 1.0×10^{-6} Am^2 magnetic dipole oriented in the y direction. (a) Simulated x component field map calculated on a 128×128 horizontal square grid at 1 mm above the sample, corresponding to a 7.5×7.5 mm^2 mapping area. (b) Estimated x component field map obtained from the map of the z component (Figure 3a). (c) Error in the estimated field map calculated as the difference between the maps shown in Figures 1a and 1b. (d) Error in the estimated map predicted by means of (49).

Taking the Fourier transform of (43) and substituting it in (13) yields

$$\hat{\tilde{b}}_x(k_x, k_y, z) = -(ik_x/k)\tilde{b}_z(k_x, k_y, z)$$
$$= -(ik_x/k)\Big[b_z(k_x, k_y, z)$$
$$- (4\pi^2)^{-1}\overline{X}(k_x, k_y) * b_z(k_x, k_y, z)\Big]$$
$$= -(ik_x/k)b_z(k_x, k_y, z) + (ik_x/k)$$
$$\cdot \Big[(4\pi^2)^{-1}\overline{X}(k_x, k_y) * b_z(k_x, k_y, z)\Big].$$

(44)

In the space domain, we have

$$\hat{\tilde{B}}_x(x, y, z) = \hat{B}_x(x, y, z) + \mathscr{F}^{-1}\{ik_x/k\} * [\overline{X}(x, y)B_z(x, y, z)]$$
$$= \hat{B}_x(x, y, z) + \Big[-x/(x^2 + y^2)^{3/2}\Big] * [\overline{X}(x, y)B_z(x, y, z)],$$

(45)

where $\mathscr{F}^{-1}\{\cdot\}$ denotes the two-dimensional inverse Fourier transform of the expression within braces. Therefore, the estimated field for a restricted mapping area is equal to the estimated field for an infinite mapping area plus an error term. The error term is given by

$$\mathscr{E}_x = \Big[-x/(x^2 + y^2)^{3/2}\Big] * [\overline{X}(x, y)B_z(x, y, z)].$$

(46)

For the typical case of rectangular and symmetrical mapping area, χ and $\overline{\chi}$ are given by

$$\chi(x, y) = \begin{cases} 1, & \text{if } |x| \le L_x/2 \text{ and } |y| \le L_y/2 \\ 0, & \text{if } |x| > L_x/2 \text{ or } |y| > L_y/2 \end{cases},$$

(47)

$$\overline{\chi}(x, y) = \begin{cases} 1, & \text{if } |x| > L_x/2 \text{ or } |y| > L_y/2 \\ 0, & \text{if } |x| \le L_x/2 \text{ and } |y| \le L_y/2 \end{cases},$$

(48)

where L_x and L_y are the dimensions of the mapping area. Hence, (46) becomes

$$\mathscr{E}_x = -\int_{-\infty}^{-L_y/2}\int_{-\infty}^{+\infty} \frac{x - x'}{\left((x - x')^2 + (y - y')^2\right)^{3/2}} B_z(x', y', z) \, dx' dy'$$
$$- \int_{L_y/2}^{+\infty}\int_{-\infty}^{+\infty} \frac{x - x'}{\left((x - x')^2 + (y - y')^2\right)^{3/2}} B_z(x', y', z) \, dx' dy'$$
$$- \int_{-L_y/2}^{+L_y/2}\int_{-\infty}^{-L_x/2} \frac{x - x'}{\left((x - x')^2 + (y - y')^2\right)^{3/2}} B_z(x', y', z) \, dx' dy'$$
$$- \int_{-L_y/2}^{+L_y/2}\int_{+L_x/2}^{+\infty} \frac{x - x'}{\left((x - x')^2 + (y - y')^2\right)^{3/2}} B_z(x', y', z) \, dx' dy'.$$
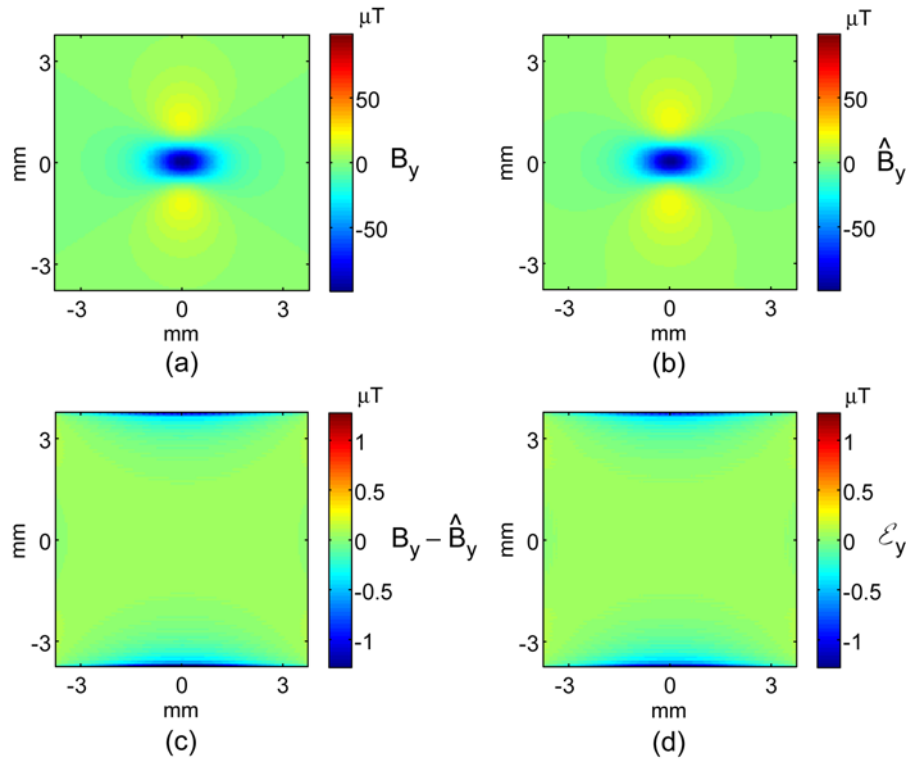
(49)

Figure 2. Results of the technique for a synthetic 1.0×10^{-6} Am^2 magnetic dipole oriented in the y direction. (a) Simulated y component field map calculated on a 128×128 horizontal square grid at 1 mm above the sample, corresponding to a 7.5×7.5 mm^2 mapping area. (b) Estimated y component field map obtained from the map of the z component (Figure 3a). (c) Error in the estimated field map calculated as the difference between the maps shown in Figures 2a and 2b. (d) Error in the estimated map predicted by means of (50).

[35] Evaluation of (49) typically requires careful use of numerical integration algorithms, as the function $-x/(x^2 + y^2)^{3/2}$ is unbounded and is also not defined at the origin. When dealing with finite-length sources, large mapping areas decrease the error, as expected, because B_z is smaller at the edges of the enlarged map.

[36] Following the same approach, error terms can be derived for the estimates of the y and z components in (12) and (15):

$$\mathcal{E}_y = \left[-y \Big/ \left(x^2 + y^2 \right)^{3/2} \right] * \left[\overline{\chi}(x,y) B_z(x,y,z) \right], \qquad (50)$$

$$\mathcal{E}_z = \left[x \Big/ \left(x^2 + y^2 \right)^{3/2} \right] * \left[\overline{\chi}(x,y) B_x(x,y,z) \right]$$
$$+ \left[y \Big/ \left(x^2 + y^2 \right)^{3/2} \right] * \left[\overline{\chi}(x,y) B_y(x,y,z) \right]. \qquad (51)$$

4.2. Discretized Map

[37] For discretized field maps, proper sampling is required to avoid information loss as well as errors in the processing of the maps. In particular, the condition established by the Nyquist-Shannon sampling theorem [*Oppenheim et al.*, 1996] should be satisfied

$$\Delta x = \Delta y = \Delta \leq \pi / k_{max}, \qquad (52)$$

where k_{max} is the maximal spatial frequency of the field component that is measured. Because most magnetic fields are not strictly band limited, some criterion should be used to define a maximum spatial frequency. We refer the reader to [*Lima et al.*, 2006] for an example of such criterion to estimate k_{max}. Because these estimates may be hard to obtain for some complex sources, one should sample the field as fine as possible, since it is always feasible to downsample a map by discarding samples in an over-sampled map. However, it is usually not possible to recover information lost by undersampling. A simple—though not infallible—way of testing whether the measurement spacing is adequate consists of computing the two-dimensional FFT of the measured map and checking whether the magnitude of the spectrum is close to zero at the highest spatial frequencies. If this happens, the map is not likely to be undersampled. In case the spectrum is nearly zero all the way down to a frequency much smaller than half the sampling rate, which is the maximum frequency observed in a digital spectrum, downsampling may be used to decrease map size. For instance, by discarding every other sample in the x and y directions, the map is downsampled in each
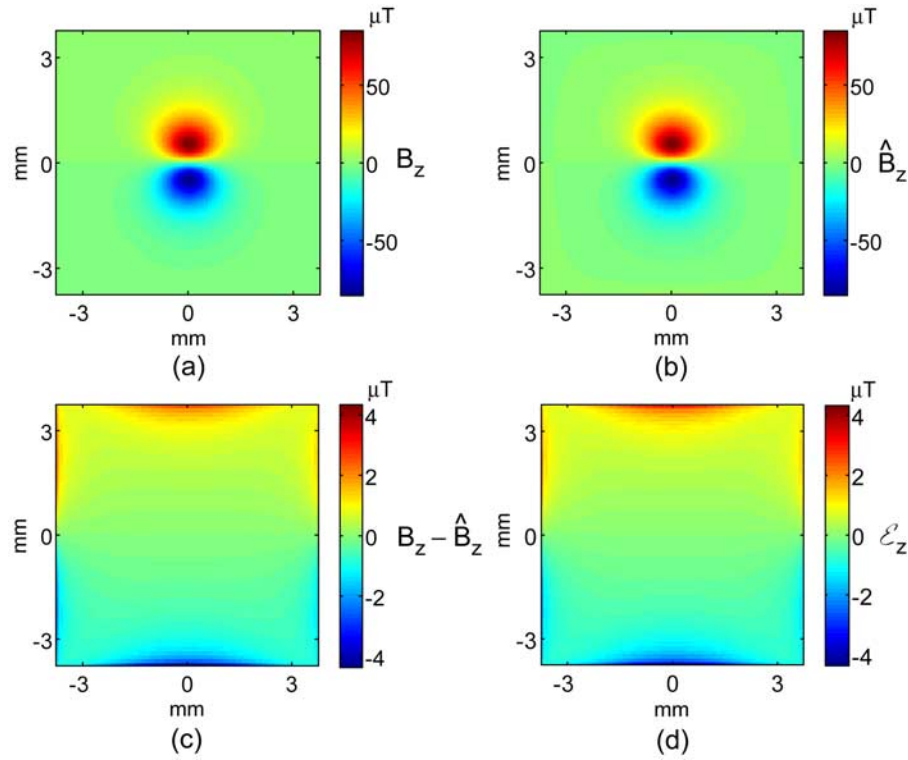
Figure 3. Results of the technique for a synthetic 1.0×10^{-6} Am^2 magnetic dipole oriented in the y direction. (a) Simulated z component field map calculated on a 128×128 horizontal square grid at 1 mm above the sample, corresponding to a 7.5×7.5 mm^2 mapping area. (b) Estimated z component field map obtained from the maps of both x (Figure 1a) and y (Figure 2a) components. (c) Error in the estimated field map calculated as the difference between the maps shown in Figures 3a and 3b. (d) Error in the estimated map predicted by means of (51).

direction by a factor of 2, which corresponds to an effective step size twice the size of the original one. However, in order to avoid aliasing, it is imperative to ensure, in this particular case, that no information is present past a quarter of the original sampling rate, or $\pi/2\Delta$.

[38] A discussion of some aspects of implementing the technique on computers is presented in Appendix B. We have utilized the software MATLAB® to implement and test our technique. Typically, we obtain accurate estimates of field maps with more than 65,000 points in just two seconds on a 3.4 GHz Dual-Core PC with 3.0-GB RAM running Windows XP in 32-bit mode.

5. Applications

5.1. Synthetic Data

[39] To test our technique and characterize its performance, we began by examining two different synthetic magnetic sources whose full vector fields we know a priori. The first was a single magnetic point dipole oriented in the y direction (Figures 1–5), and the second was an extended magnetization distribution composed of strips in the shape of the Massachusetts Institute of Technology's logo that are uniformly magnetized in the $\pm z$ directions (Figure 6). In Figures 1–10, the orientation of the coordinate axes follows the one adopted in Figure 1. We utilized the normalized root-mean-square deviation (NRMSD) to quantify the discrepancies between actual and estimated maps:

$$\text{NRMSD} = \left[\frac{\int_{-\infty}^{+\infty} \int_{-\infty}^{+\infty} |\hat{f}(x,y,z) - f(x,y,z)|^2 \, dx dy}{\int_{-\infty}^{+\infty} \int_{-\infty}^{+\infty} |f(x,y,z)|^2 \, dx dy} \right]^{1/2}, \quad (53)$$

where $\hat{f}$ represents an estimated field map, and f stands for the actual field map.

[40] Figures 1a, 2a, and 3a show the x, y, and z components, respectively, of the magnetic field of a 1.0×10^{-6} Am^2 magnetic dipole oriented in the y direction measured on a 128×128 horizontal square grid (7.5×7.5 mm^2) at a distance of 1 mm above the sample. The recovered map of the x component, obtained from the map of the z component (Figure 3a) by means of (13) and (17), is presented in Figure 1b. Figure 1c shows the error in the estimate, that is, the difference between the two field maps shown in Figures 1a and 1b. We notice that the error is quite small (maximum error of ~1.3% of the peak field value, NRMSD = 7.66×10^{-3}), and it is larger near the edges of the map. To investigate the source of this small discrepancy between the original field map and the estimated map,
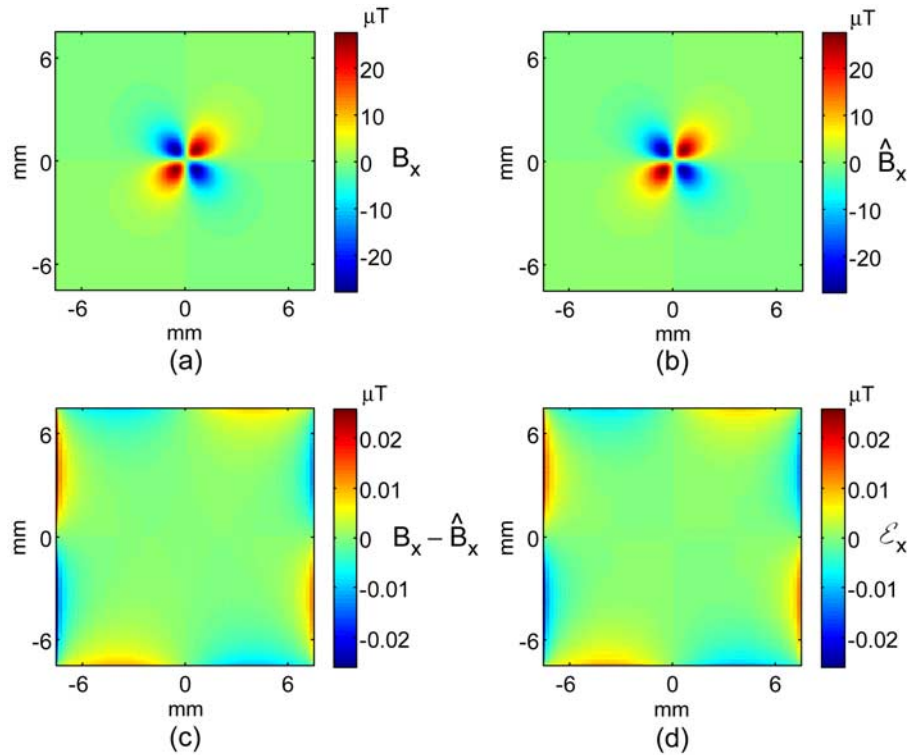
Figure 4. Results of the technique for a synthetic 1.0×10^{-6} Am^2 magnetic dipole oriented in the y direction. (a) Simulated x component field map calculated on an extended 256×256 horizontal square grid at 1 mm above the sample, corresponding to a 15×15 mm^2 mapping area. (b) Estimated x component field map obtained from an extended map of the z component (not shown). (c) Error in the estimated field map calculated as the difference between the maps shown in Figures 4a and 4b. (d) Error in the estimated map predicted by means of (49).

we computed the error distribution due to a restricted mapping area, as given by (49). The predicted error distribution is presented in Figure 1d. We can see that the agreement between the actual and predicted errors is excellent. This indicates that the actual numerical error of the estimation technique is quite small compared to the error associated with reduced mapping areas.

[41] Figure 2a shows the y component of the field produced by the same magnetic dipole, and the recovered field using (12) and (18) is presented in Figure 2b. The error in the recovered component and the predicted error are shown in Figures 2c and 2d, respectively. The maximum error was again ~1.3% of the peak field value, while the NRMSD was 1.17×10^{-2}.

[42] Next, we estimated the z component of the field based on the x (Figure 1a) and y (Figure 2a) component maps, by means of (15), (17), and (18). Figure 3a shows the z component of the field produced by the same magnetic dipole as before, while Figure 3b shows the estimated z component map. Figures 3c and 3d show the recovery error and the predicted error, respectively. Once again, a very good agreement between theoretical and recovered field components was obtained. The maximum error was ~5.1% of the peak field (NRMSD = 5.49×10^{-2}) and it was concentrated near the edges of the map. This larger error is not surprising, considering that the map of the x component

(Figure 1a), which is used in the calculations, is somewhat extended. Because the field is larger at the boundaries of the mapping area, the recovery error increases accordingly, as given by (51).

[43] In order to verify that the recovery error indeed decreases substantially as the mapping area is enlarged, we doubled the dimensions of the mapping region while keeping the same discretization (step size). Figure 4a shows a map of the x component of the field of the same dipole used previously, calculated on a 256×256 horizontal square grid (15×15 mm^2) located 1 mm above the sample. The map of the recovered x component is presented in Figure 4b, while the recovery error and the predicted error are shown in Figures 4c and 4d, respectively. The maximum error was 0.094% of the peak field value (NRMSD = 1.05×10^{-3}), located at the edges of the map. Similar error level reductions were obtained for the recovered y and z components (recovered maps not shown): 0.091% (NRMSD = 1.62×10^{-3}) and 0.73% (NRMSD = 1.51×10^{-2}), respectively. Again, the error in the recovered z component was several times greater than the error in the estimated x and y components.

[44] We then proceeded to investigate the effects of sensor noise on the recovered maps. As mentioned before, noise levels in estimated field components are expected to be smaller than in primary field maps used in the estimation
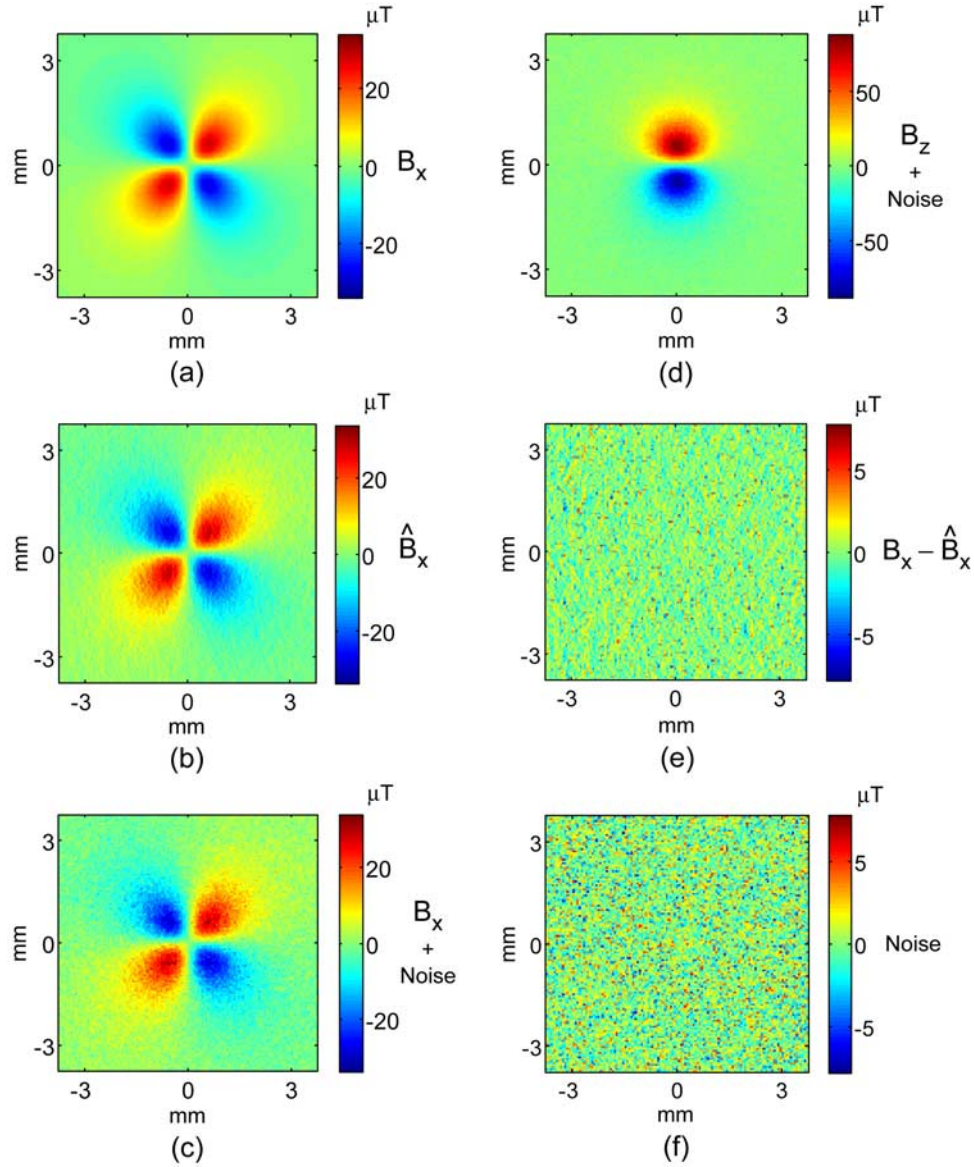
Figure 5. Effects of noise on estimated field maps for a synthetic 1.0×10^{-6} Am^2 magnetic dipole oriented in the y direction. (a) Noiseless x component field map calculated on a 128×128 horizontal square grid at 1 mm above the sample, corresponding to a 7.5×7.5 mm^2 mapping area. (b) Estimated x component field map obtained from the z component map corrupted by a large amount of additive noise (shown in Figure 5d). (c) Noiseless x component field map corrupted by the same amount of additive noise as the z component shown in Figure 5d, corresponding to equivalent levels of simulated sensor noise. Note that the estimated x component shown in Figure 5b is actually less noisy than this field map with simulated sensor noise. (d) Noisy z component field map obtained by adding white noise (shown in Figure 5f) to the noiseless z component map shown in Figure 5a to simulate sensor noise, resulting in a signal-to-noise ratio of 16.8 dB. (e) Effective noise present in the estimated x component map shown in Figure 5b. (f) White noise component simulating sensor noise.

process owing to the low-pass filtering effect intrinsic to the technique. Notice that this does not necessarily imply a better signal-to-noise ratio (SNR), as differences in amplitude of one field component relative to another may, in fact, reduce the overall SNR of a recovered component even if the noise level is decreased by the processing. Because sensor noise is usually not correlated with the field source, such reduction in SNR may also occur in actual mappings of components using magnetometers. We adopted the following definition of SNR:

$$SNR = 10 \log_{10} \frac{\displaystyle\int_{-\infty}^{+\infty} \int_{-\infty}^{+\infty} |s(x,y)|^2 dxdy}{\displaystyle\int_{-\infty}^{+\infty} \int_{-\infty}^{+\infty} |\eta(x,y)|^2 dxdy} \ \text{dB}, \qquad (54)$$

where s denotes the (noiseless) signal, or field component in this case, and η stands for the noise spatial distribution. It is essentially the ratio between the energy of the signal and the energy of the noise, expressed in decibels.

[45] We used the same magnetic dipole as that in Figures 1–3 to test the noise performance of the technique. High noise levels were introduced to highlight the effects of noise contamination, as well as to demonstrate that the technique is robust and performs well under adverse conditions. We added Gaussian white noise (shown in Figure 5f)

to the z component of the field (see Figure 3a), resulting in a SNR of 16.8 dB. This corresponds to a ratio of $\sim$48 between the energy of the field map and the energy of the noise spatial distribution or, in this particular case, to peak field $\sim$11 times larger than the peak noise. This noisy primary field map is shown in Figure 5d, while the noiseless synthetic x component of the field is shown in Figure 5a. Figure 5b shows the estimated x component field map obtained from the noisy z component; the resulting estimate has a SNR of 14.0 dB. For comparison, Figure 5c displays
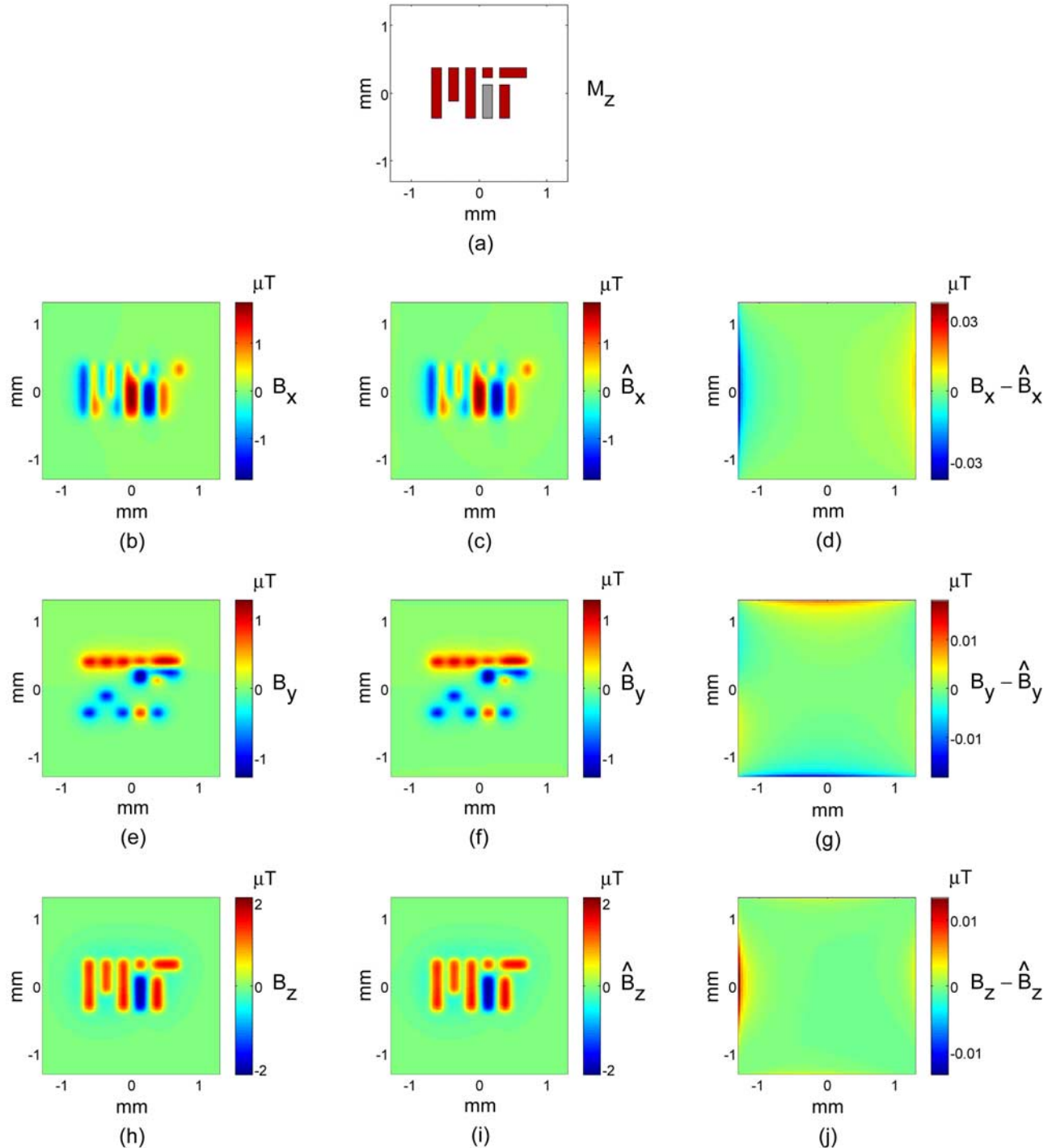

Figure 6

the noiseless x component corrupted with the same amount of additive noise as the primary field shown in Figure 5d, simulating a measured x component map contaminated by sensor noise. Such a field map has a SNR of only 10.8 dB, which is 3.2 dB ($\sim$ a factor of 2) worse than the SNR of the recovered field map. A closer look reveals that the estimated x component is indeed less noisy than what would be measured by a magnetometer. Since the noiseless map is known in this case, we can separate the noise in the recovered field (shown in Figure 5e), which includes the error associated with reduced mapping areas. By comparing Figures 5e and 5f, one can see that 5e is a low-pass filtered version of 5f. In fact, the standard deviation of the noise in Figure 5e is 1.45 μT, whereas the standard deviation of the noise in Figure 5f is 2.06 μT.

[46] The second synthetic field source tested was more complex: uniformly magnetized flat slabs in the shape of the Massachusetts Institute of Technology (MIT) logo, as shown in Figure 6a. All slabs are magnetized in the $+z$ direction (out of the plane), except for the main part of the "I" letter, which is magnetized in the $-z$ direction (into the plane). The magnetization intensity is 800×10^{-6} A/m for all slabs. Synthetic field maps of the x, y, and z components, shown in Figures 6b, 6e, and 6h, respectively, were calculated on a 128×128 grid (2.6×2.6 mm^2) at a distance of 100 μm from the sample. The x and y component recovered field maps, obtained from the map of the z component, are shown in Figures 6c and 6f, respectively, while the corresponding recovery errors are shown in Figures 6d and 6g. The maximum errors were 2.02% and 1.41% of the peak field values, respectively (corresponding NRMSDs were 1.24×10^{-2} and 1.11×10^{-2}). Figure 6i shows the recovered z component magnetic field map, obtained from the synthetic maps of the x and y components, while the associated recovery error is shown in Figure 6j. The maximum error was 1.64% of the peak field value, and the NRMSD was 5.66×10^{-2}. Once again, the recovered fields exhibited excellent agreement with the theoretical calculations.

5.2. Experimental Data

[47] We used four different samples and two magnetic sensors to test and demonstrate our technique applied to real magnetic field maps. Our first sample consisted of a flexible magnet commonly found at hardware stores that was cut across into small strips and glued onto a plastic board so as to form the shape of the MIT logo (Figure 7a). Each strip exhibits an alternating pole magnetization pattern, resembling a "caterpillar." We mapped the three components of the magnetic field using a Hall-effect magnetometer (Magnetic Instrumentation, Inc., Model 2100 Gaussmeter) equipped with both axial (for measuring the z component) and transverse (for measuring both x and y components) probes. All measurements were performed outside of a shielded room under adverse noise conditions owing to the proximity of the magnetic sensor to computers and various lab equipment. A custom-built x-y scanning stage with high-precision piezoceramic motors and submicron accuracy, which is part of our SQUID microscope system, was used to move the sample underneath the Hall probe. A custom LabVIEW program controlled the x-y stage as well as a digital acquisition board, producing the z, x, and y component field maps shown in Figures 7b, 7e, and 7g, respectively. Because different probes had to be used to map all three components of the field, and since the transverse probe had to be rotated by 90° in order to measure the second horizontal field component, we could not ensure a constant sensor-to-sample distance and an accurate alignment of the three maps. In particular, because the Hall elements are not situated at the same distance from the tip of the probes, a noticeable decrease in spatial resolution was observed in our measurements of the x and y components (Figures 7e and 7g, respectively) when compared to the map of the z component (Figure 7b). This is an example of the difficulties encountered with vector mapping systems described in section 1.

[48] After mapping the three components, we used our technique to estimate the x and y component maps from the z component map only. The estimated B_x is shown in Figure 7c, while the estimated B_y is shown in Figure 7d. Notice that these estimated maps correspond to the same sensor-to-sample distance as the z component map (Figure 7b). Direct comparison of Figures 7c and 7e and of Figures 7d and 7g demonstrates that the recovered horizontal component maps have much higher spatial resolution than the measured maps. In order to properly compare the estimated and measured maps to check the accuracy of our calculations, we used upward continuation [Blakely, 1996] to bring the estimated maps to the same sensor-to-sample distances corresponding to the real maps of the x and y components. The estimated x component map upward continued by 2.1 mm is shown in Figure 7f, while the estimated y component map upward continued by 2.3 mm is presented in Figure 7h. (These distances are

---

Figure 6. Results of the technique for a synthetic magnetization distribution in the shape of the Massachusetts Institute of Technology (MIT) logo. (a) Magnetization distribution composed of rectangular strips uniformly magnetized in the $\pm z$ direction. Red indicates magnetization oriented in the $+z$ direction (out of the plane), while gray represents magnetization oriented in the $-z$ direction (into the plane). All strips have magnetization intensities of 800 μA/m. (b) Simulated x component field map calculated on a 128×128 horizontal grid (2.6×2.6 mm^2) at a distance of 100 μm from the sample. (c) Estimated x component field map obtained from the map of the z component shown in Figure 6h. (d) Error in the estimated field map calculated as the difference between the maps shown in Figures 6b and 6c. (e) Simulated y component field map calculated on a 128×128 horizontal grid (2.6×2.6 mm^2) at a distance of 100 μm from the sample. (f) Estimated y component field map obtained from the map of the z component shown in Figure 6h. (g) Error in the estimated field map calculated as the difference between the maps shown in Figures 6e and 6f. (h) Simulated z component field map calculated on a 128×128 horizontal grid (2.6×2.6 mm^2) at a distance of 100 μm from the sample. (i) Estimated z component field map obtained from the maps of both x and y components shown in Figures 6b and 6e, respectively. (j) Error in the estimated field map calculated as the difference between the maps shown in Figures 6h and 6i.
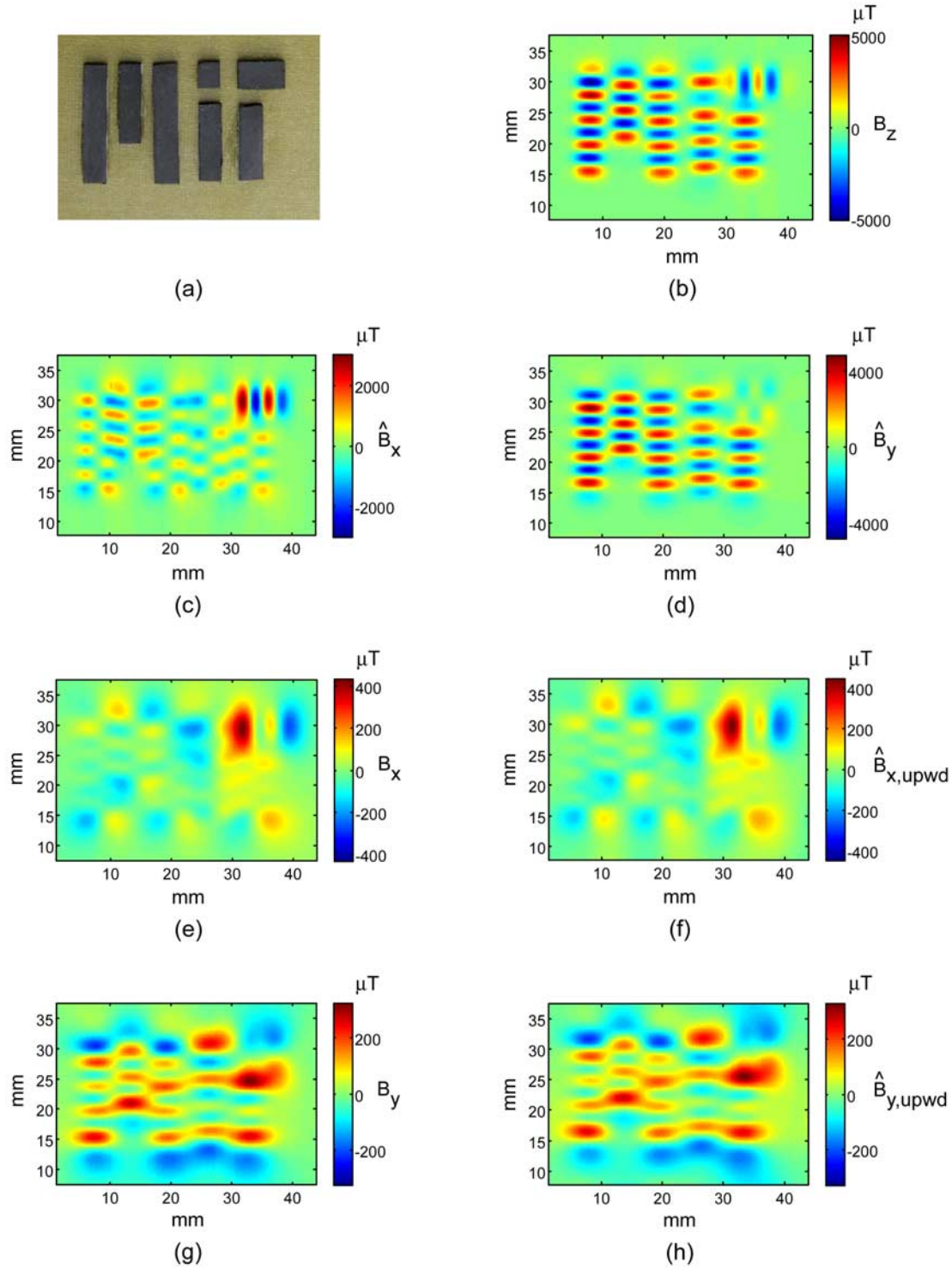
Figure 7. Experimental results of the technique for a test sample composed of strips of flexible magnet arranged in the shape of the MIT logo. (a) Photograph of the test sample. (b) Map of the z component of the magnetic field of the sample measured by a Hall-effect magnetometer at an effective sensor-to-sample distance of ∼2 mm. (c) Estimated x component field map obtained from the map of the z component shown in Figure 7a. (d) Estimated y component field map obtained from the map of the z component shown in Figure 7a. (e) Map of the x component measured by a Hall-effect magnetometer at an effective distance of ∼4.1 mm from the sample. (f) Estimated x component field map (Figure 7c) upward continued by 2.1 mm to match the experimental sensor-to-sample distance. (g) Map of the y component measured by a Hall-effect magnetometer at an effective distance of ∼4.3 mm from the sample. (h) Estimated y component field map (Figure 7d) upward continued by 2.3 mm to match the experimental sensor-to-sample distance. Notice the excellent agreement between Figures 7e and 7f and Figures 7g and 7h.
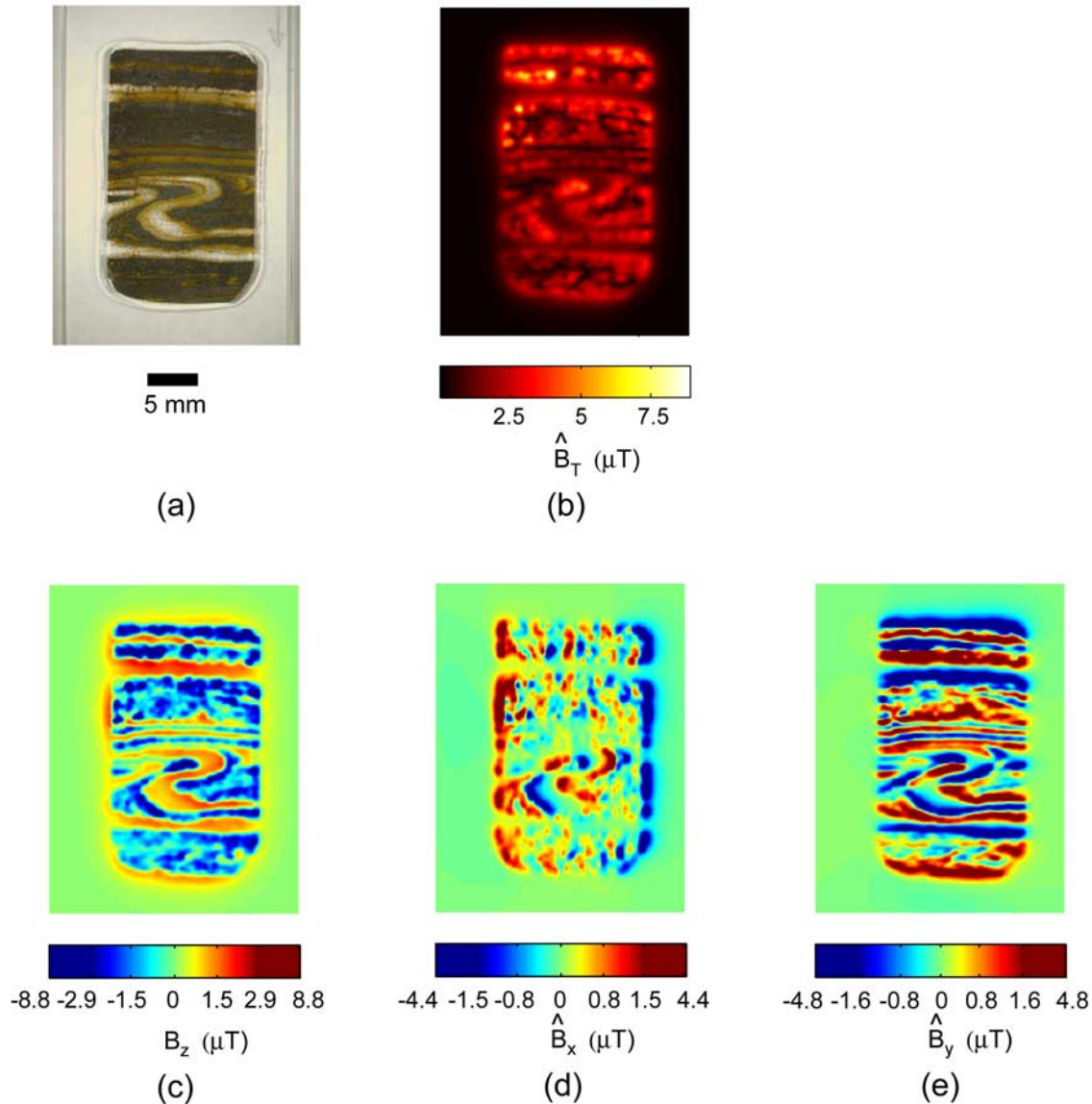
Figure 8. Experimental results of the technique for a 100-μm thin section of a microfolded Archean hematite-bearing banded iron formation from the Jack Hills, Western Australia. (a) Reflected light photograph of the sample. (b) Total field map calculated from Figures 8c–8e. (c) Map of the z component of the natural remanent field of the sample measured by our SQUID microscope at a sensor-to-sample distance of ~450 μm. (d) Estimated x component field map obtained from the map of the z component shown in Figure 8c. (e) Estimated y component field map obtained from the map of the z component shown in Figure 8c. Color scales in Figures 7c–7e were saturated to emphasize small features.

consistent with the differences in probe design, as well as with the uncertainty associated with repositioning the probe over the sample after a rotation.) Comparisons of Figures 7e and 7f, and of Figures 7g and 7h show excellent agreement between measured and estimated components of the magnetic field, with only minor differences. Owing to the uncertainties in probe repositioning, it was not possible in this case to obtain an assessment of the recovery error by means of subtracting the estimated map from the actual field map. Imprecision in the alignment of the two maps creates artifacts that dominate the error spatial distribution. This, in fact, highlights another advantage of the technique, especially when obtaining estimates based on a single

component: the estimated maps have the same origin, orientation and sample-to-sensor distance as the original map, which is something that cannot be achieved in real maps since two sensors cannot occupy the same place in space (or, in the case of subsequent measurements, cannot be brought to the exact same position relative to the sample). In certain applications, such as inverse problems, these registration issues can be critical.

[49] Next, we applied our technique to magnetic maps of three geological samples. Our focus is to demonstrate the applicability and performance of the technique, whereas it is beyond the scope of this paper to conduct detailed paleomagnetic analyses on these samples. Instead, we illustrate
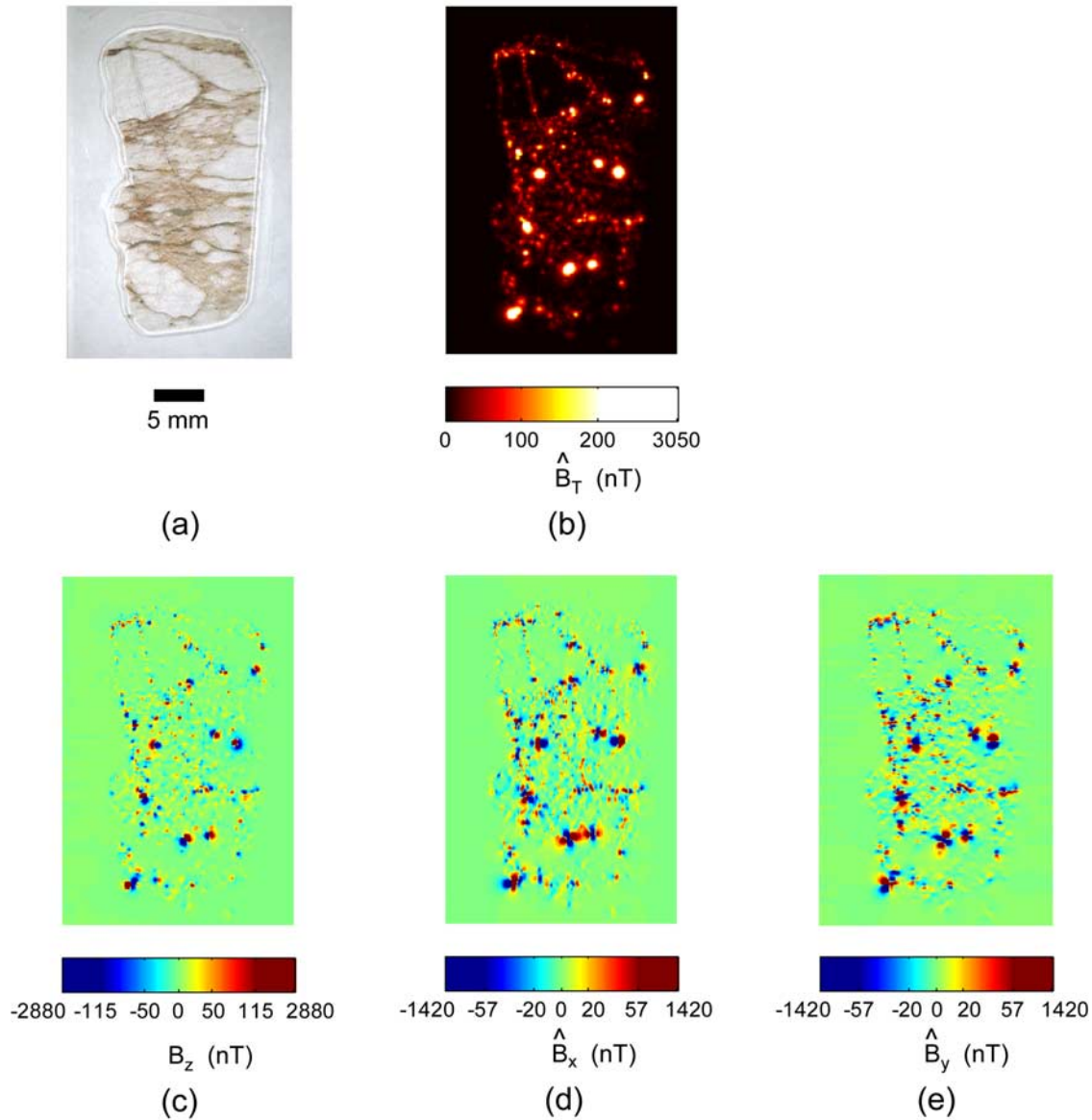
Figure 9. Experimental results of the technique for a 100-μm thin section of an Archean hematitic quartz-pebble conglomerate from the Jack Hills, Western Australia. (a) Reflected light photograph of the sample. (b) Total field map calculated from Figures 9c–9e. (c) Map of the z component of the natural remanent field of the sample measured by our SQUID microscope at sensor-to-sample distance of $\sim$215 μm. (d) Estimated x component field map obtained from the map of the z component shown in Figure 9c. (e) Estimated y component field map obtained from the map of the z component shown in Figure 9c. Color scales in Figures 9b–9e were saturated to emphasize small, weak features.

the potential of vector maps, and indicate how these data may be eventually incorporated into the analysis of geological samples.

[50] We used our SQUID microscope system, which is housed in a three-layer mu metal can situated inside a two-layer mu metal shielded room with active compensation coils, to map the z component of the remanent magnetic field from a 100-μm thin section of a microfolded Archean hematite-bearing banded iron formation from the Jack Hills, Western Australia [*Spaggiari et al.*, 2007]. Figure 8a shows a reflected light photograph of the thin section, where the microfold can be easily observed. Figure 8c shows the map of the z component of the natural remanent field mea-

sured by the SQUID microscope at a sensor-to-sample distance of approximately 450 μm. On the basis of this map, we calculated the x and y component maps shown in Figures 8d and 8e, respectively. We have saturated the color scale in all the individual component maps so as to emphasize small features present in the underlying magnetization distribution. Figure 8b shows the total field map computed from 8c, 8d, and 8e. Comparison of Figures 8a and 8b allows us to associate field strength with features present in the sample, which potentially indicates which minerals carry most magnetization. This kind of information can greatly constrain the magnetic inverse problem, as source elements can be eliminated from regions of low field
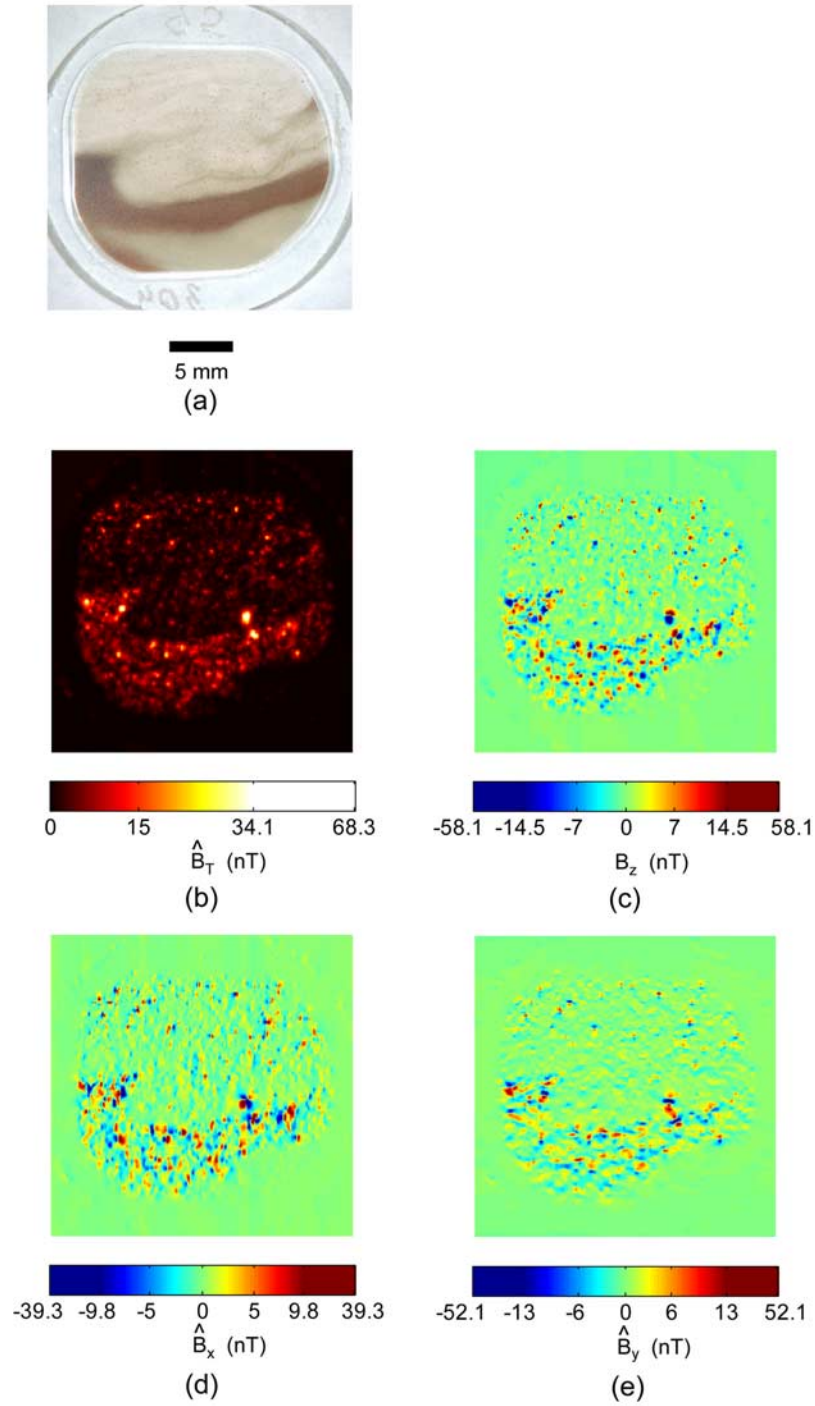
Figure 10. Experimental results of the technique for a 30-μm thin section of a microfolded magnetite- and hematite-bearing limestone from the Neoproterozoic Svanbergfjellet Formation, Svalbard. (a) Reflected light photograph of the sample. (b) Total field map calculated from Figures 10c–10e. (c) Map of the z component of the natural remanent field of the sample measured by our SQUID microscope at sensor-to-sample distance of $\sim$215 μm. (d) Estimated x component field map obtained from the map of the z component shown in Figure 10c. (e) Estimated y component field map obtained from the map of the z component shown in Figure 10c. Color scales in Figures 10b–10e were saturated to emphasize small, weak features.

strength. This not only reduces the size of the inverse problem, but actually improves the quality of the solution by requiring recovered magnetization distributions that closely match the sample's geometric and magnetic characteristics. Qualitative analysis of the individual component maps may also bring out interesting information regarding general aspects of the magnetization. For instance, a first step to carry out a fold test on this sample would consist of rejecting the hypothesis of unidirectional magnetization. In fact, our preliminary inversions using the three-component maps (not shown) assuming a unidirectional magnetization distribution model failed to adequately explain the magnetic field around the microfold.

[51] We then mapped the z component of the natural remanent magnetic field of a 100-μm thin section of an Archean hematitic quartz-pebble conglomerate from the
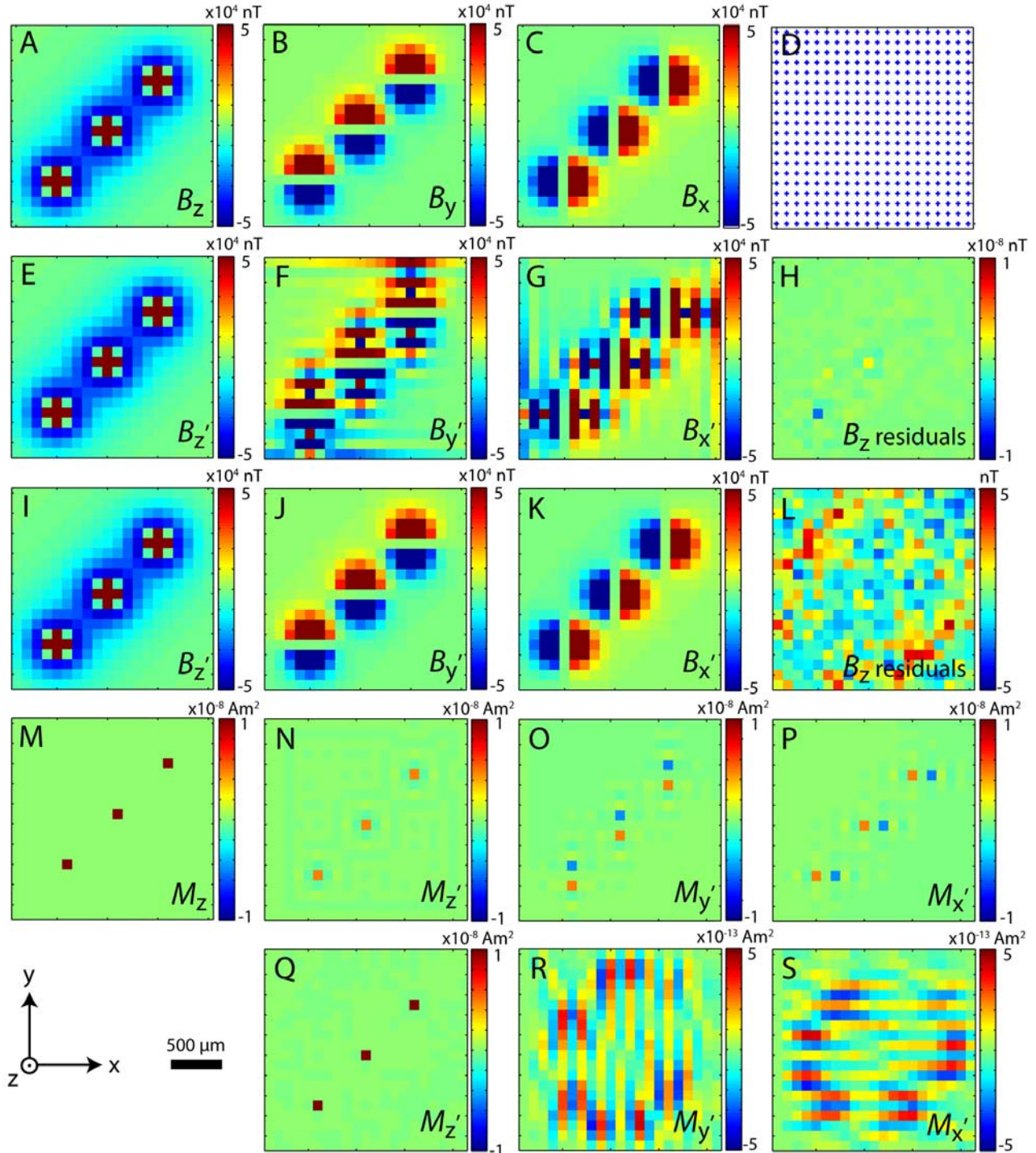

Figure A1

Jack Hills, Western Australia [*Spaggiari et al.*, 2007] with our SQUID microscope at a sensor-to-sample distance of 215 μm (Figure 9c). Figure 9a shows the reflected light photograph of the sample, while Figures 9d and 9e show the estimated maps of the x and y components, respectively. The total field map is shown in Figure 9b. The color scales in Figures 9b–9e were saturated to enhance weaker sources. A comparison between the total field map and reflected light photograph shows about a dozen spots mainly associated with hematite staining that generate strong fields. Analysis of the individual component maps reveal that these "hot spots" clearly exhibit a dipolar behavior and are magnetized in different directions. We also notice a multitude of small weaker features of dipolar nature with scattered magnetization directions.

[52] Finally, we scanned a 30-μm thin section of a microfolded magnetite- and hematite-bearing limestone from the Neoproterozoic Svanbergfjellet Formation, Svalbard [*Maloof et al.*, 2006] with our SQUID microscope again at a sensor-to-sample distance of 215 μm. Figure 10a shows the reflected light photograph of the sample, and Figure 10c shows the z component field recorded by the microscope. On the basis of this map, the x (Figure 10d) and y (Figure 10e) component maps were estimated. The total field map shown in Figure 10b was computed from the three individual component maps. In this case, the total field map shows only a few spots with field strength above the average, and we clearly notice two regions of distinct field strengths: the pink oxide-rich region at bottom, which has stronger field strengths, and the light-colored remainder of the sample which is associated with slightly weaker fields.

6. Conclusions

[53] We summarize below the main features of our technique:

[54] 1. We have developed an improved technique in the Fourier domain that retrieves planar vector field maps from a single-component map of the magnetic field external to a geological sample. No assumptions are made regarding the sources of magnetic field other than (1) the existence of a half-space devoid of sources where the field is measured and the estimates are calculated and (2) time derivatives of the magnetic field fields can be neglected. This technique is adapted to the requirements and peculiarities of scanning magnetometry.

[55] 2. Assumptions and constraints imposed on magnetic field distributions that, in many situations, precluded the use of similar techniques in the Fourier domain formulated for geomagnetic anomaly data can be easily satisfied in scanning magnetometry.

[56] 3. By properly characterizing the singularities in the method's equations and their associated discontinuities, we established what the best sensor and mapping configurations are.

[57] 4. Measuring the magnetic field component normal to the scanning plane and subsequently recovering the field components parallel to this plane yields the best results. This is the optimal scanning magnetometer configuration for obtaining vector field maps.

[58] 5. The technique is fast and robust, and there is no amplification of noise. On the contrary, we showed the estimated components have less noise than the primary single-component map.

[59] 6. The major source of error is associated with the dimensions of the mapping area. An excessively reduced mapping area results in cropped field maps and increased error in the estimated components. We provided formulas to quantify this error. The numerical error of the technique is negligible.

[60] 7. It is possible to obtain vector field maps with virtually no information loss by choosing suitable mapping areas that include regions sufficiently away from the sample where the total field is known to be effectively zero. Using synthetic data, we demonstrated that estimated maps with error levels below 0.1% of the peak field can be easily obtained with realistic mapping area dimensions.

[61] 8. Three-component measurements made with a commercial Hall sensor magnetometer confirmed the excellent agreement between estimated and actual field component maps using experimental data obtained in a noisy environment.

[62] 9. Maps of the vertical component of the natural remanent field of three geological samples measured with our SQUID microscope were used to calculate vector field maps. We illustrated how total field maps can be used to correlate field strength with petrographic textures in the sample, and that this information can be used to distribute source elements of an inverse problem model. We also

Figure A1. Comparison of magnetization retrieval from modeled magnetic microscopy data using both single-component (only B_z) and three-component data (using B_z, B_y, and B_x). Model field data (nT) of (a) B_z, (b) B_y, and (c) B_x. (d) Positions of each of 400 dipoles arranged in a 20×20 grid used to model field data (marked with crosses). Synthetic data (nT) of (e) $B_z{'}$, (f) $B_y{'}$, and (g) $B_x{'}$ retrieved from least squares fits to B_z only (i.e., using Figure A1a). (h) B_z residuals from least squares fits to B_z only (i.e., data in Figure A1a minus data in Figure A1e). Synthetic data (nT) of (i) $B_z{'}$, (j) $B_y{'}$, and (k) $B_x{'}$ retrieved from least squares fits using B_z, B_y, and B_x simultaneously (i.e., using Figures A1a–A1c). (l) B_z residuals from least squares fits to B_z, B_y, and B_x (i.e., data in Figure A1a minus data in Figure A1i). (m) True magnetization (Am^2) oriented out of the page: three dipoles each with moment $M_z = 1 \times 10^{-8}$ Am^2 and $M_y = M_x = 0$ (not shown). The magnetic fields of these sources are the model data in Figures A1a–A1c. Magnetization solution (Am^2) retrieved using B_z only (i.e., using Figure A1a): (n) $M_z{'}$, (o) $M_y{'}$, and (p) $M_x{'}$. This solution was used to forward model data in Figures A1e–A1g. Magnetization solution (Am^2) retrieved using B_z, B_y, and B_x (i.e., using Figures A1a–A1c) for (q) $M_z{'}$, (r) $M_y{'}$, and (s) $M_x{'}$. This solution was used to forward model data in Figures A1i–A1k. Note that intensity scales for B_z residuals in Figures A1h and A1l differ from one another by 8 orders of magnitude and are both orders of magnitude lower than synthetic data (Figures A1e and A1i). Note also that intensity scales for $M_y{'}$ and $M_x{'}$ in Figures A1r and A1s are more than 4 orders of magnitude smaller than Figures A1o and A1p. As shown at lower left, z = out of the page, y = bottom to top, x = left to right.

showed that visual inspection of the three component maps may reveal general attributes of the magnetization distribution.

[63] 10. Because the quality of the estimated maps is excellent, our technique shows that it is often more advantageous to have a single-axis magnetometer with high spatial resolution than a vector magnetometer with moderate spatial resolution, particularly in magnetic scanning microscopy. Specifically, our example using a Hall sensor magnetometer shows that the estimated horizontal component maps exhibit much better spatial resolution than the corresponding measured maps.

Appendix A: Advantages of Vector Data for Studying Remanent Magnetization: A Simple Example

[64] We demonstrate the advantages of three-component data over single-component data for magnetic microscopy imaging of remanent magnetization with a simple example. Our goal is determine the magnetization pattern of three upwardly oriented magnetic dipoles (Figure A1m) from synthetic field measurements as might be obtained with a typical SQUID microscope (Figures A1a–A1c). The dipoles are situated in a plane at 0.1 mm below a model SQUID microscope sensor which measures their fields in a planar grid of 400 locations with spacing of 0.1 mm (Figure A1d). In the following discussion, we refer to these field maps as the ''model data'' (B) and the magnetization that generated them as the ''true magnetization'' (M_z). Using an equivalent source scheme solved using the conjugate gradient analysis routine LSQR [*Paige and Saunders*, 1982], we fit for the three components of the magnetization solution (M_z', M_y', M_x') which best reproduces the model data (Figures A1e–A1l). Each dipole was allowed to independently vary in direction and magnitude. For these calculations, we retained the full (untruncated and nonsparse) Jacobian and the LSQR iterations were terminated when the solution approached a stable value and before any signs of overfitting (e.g., growth in solution norm with little improvement in residuals). We conducted this inversion in two ways: using only the z component model data, B_z (i.e., Figure A1a) and then again using all three field components B_z, B_y, and B_x (i.e., Figures A1a–A1c). Finally, we calculated the magnetic field produced by each of these solutions (we refer to these fields as ''synthetic data,'' B') (Figures A1e–A1g, A1i–A1k). For the three-component fits, the number of unknown parameters $P = 1200$ (400 dipoles × 3 components each) is equal to the number of data points N (field measured at 400 locations × 3 components), whereas the single-component fits have $P = 1200$ and $N = 400$, and are severely underdetermined.

[65] We found that both synthetic data sets B_z' are in excellent agreement with the model. The single-component fit has B_z residuals that are orders of magnitude lower than the three-component fit because it is optimized to matching this field component (whereas the three-component fits minimize the residuals for all three components). However, the superior fitting by the single-component method has a cost: it leads to a magnetization solution (Figures A1n–A1p) which is far more inaccurate than that of the three-component fits (Figures A1q–A1s) and which poorly

reproduces B_y and B_x (compare Figures A1f and A1g and Figures A1j and Figures A1k to Figures A1b and Figures A1c). This difference in fitting is not due to a nonoptimal choice of the number of conjugate gradient iterations used to obtain the final solutions: we found that the high-frequency structure visible in Figures A1n–A1p sets in at small iteration numbers and that there is no optimal iteration number which can regularize these solutions. This simple example shows how even in a case where numerical noise is the sole noise source, knowledge of all three components of the magnetic field can provide more accurate constraints on magnetization sources compared to that of just a single field component.

Appendix B: Practical Implementation

[66] Although numerical implementation of our technique on computers is straightforward, some aspects require particular attention so as to avoid inaccuracies in the calculations. The most important issue is ensuring that expressions such as (17) and (18) are sampled precisely in the same way as the DFT/FFT algorithm samples the spectrum of the field maps. In this way, we guarantee that proper weights are applied at each spatial frequency when performing multiplications between the spectra of the field components and the filter functions in (12), (13), and (15). This is a crucial step to achieve low error levels in the estimates. Because the discrete time Fourier transform is a periodic function, the sampling scheme in the frequency domain may vary depending on the implementation of the DFT/FFT algorithm used. A nonnegligible imaginary component resulting from an inverse Fourier transform operation, for instance, is a strong indication that something was not done correctly in the calculations.

[67] Another point that may contribute to errors in the estimated component maps is coarse sampling of the spectrum by the DFT/FFT algorithm. We strongly suggest the use of zero-padding techniques [*Marple*, 1987] to tackle this problem, especially when the number of points in the map is small. Clearly, sampling the spectrum too finely leads to very large matrices, which should also be avoided owing to long computation times and high memory requirements. Thus, a practical approach consists of doubling the number of points in each dimension by means of zero padding and checking whether the new estimates display any noticeable changes. If they do, we repeat the procedure by quadrupling the number of points, and so on, until no significant differences are observed or until the matrices get too large.

References

Arturi, C. M., L. Di Rienzo, and J. Haueisen (2004), Information content in single-component versus three-component cardiomagnetic fields, *IEEE Trans. Magn.*, *40*, 631–634, doi:10.1109/TMAG.2004.824891.

Bhattacharyya, B. K. (1977), Reduction and treatment of magnetic anomalies of crustal origin in satellite data, *J. Geophys. Res.*, *82*, 3379–3390, doi:10.1029/JB082i023p03379.

Blakely, R. J. (1996), *Potential Theory in Gravity and Magnetic Applications*, 441 pp., Cambridge Univ. Press, New York.

Bracewell, R. N. (1999), *The Fourier Transform and its Applications*, 640 pp., McGraw-Hill, New York.

Bradshaw, L. A., J. K. Ladipo, D. J. Staton, J. P. Wikswo, and W. O. Richards (1999), The human vector magnetograstrogram and magnetoenterogram, *IEEE Trans. Biomed. Eng.*, *46*, 959–970, doi:10.1109/10.775406.

Di Rienzo, L., J. Haueisen, and C. M. Arturi (2005), Three component magnetic field data, *Compel*, *24*, 869–881.

Egli, R., and F. Heller (2000), High-resolution imaging using a high-T_c superconducting quantum interference device (SQUID) magnetometer, *J. Geophys. Res.*, *105*, 25,709–25,727, doi:10.1029/2000JB900192.

Fong, L. E., J. R. Holzer, K. K. McBride, E. A. Lima, F. Baudenbacher, and M. Radparvar (2005), High-resolution room-temperature sample scanning superconducting quantum interference device microscope configurable for geological and biomagnetic applications, *Rev. Sci. Instrum.*, *76*, 053703, doi:10.1063/1.1884025.

Galliher, S. C., and M. A. Mayhew (1982), On the possibility of detecting large-scale crustal remanent magnetization with MAGSAT vector magnetic anomaly data, *Geophys. Res. Lett.*, *9*, 325–328.

Hinojosa, J. H., and K. L. Mickus (2002), Hilbert transform of gravity gradient profiles: Special cases of the general gravity-gradient tensor in the Fourier transform domain, *Geophysics*, *67*, 766–769, doi:10.1190/1.1484519.

Hughes, D. S., and W. L. Pondrom (1947), Computation of vertial magnetic anomalies from total magnetic field measurements, *Eos Trans. AGU*, *28*, 193–197.

Ketchen, M. B., J. R. Kirtley, and M. Bhushan (1997), Miniature vector magnetometer for scanning SQUID microscopy, *IEEE Trans. Appl. Supercond.*, *7*, 3139–3142, doi:10.1109/77.621997.

Langel, R. A., and W. J. Hinze (1998), *The Magnetic Field of the Earth's Lithosphere*, 429 pp., Cambridge Univ. Press, Cambridge, U. K.

Langel, R. A., C. C. Schnetzler, J. D. Phillips, and R. J. Horner (1982), Initial vector magnetic anomaly map from MAGSAT, *Geophys. Res. Lett.*, *9*, 273–276, doi:10.1029/GL009i004p00273.

Lima, E. A., A. Irimia, and J. P. Wikswo (2006), The magnetic inverse problem, in *The SQUID Handbook*, edited by J. Clarke and A. I. Braginski, pp. 139–267, Wiley-VCH, Weinheim, Germany.

Lourenco, J. S., and H. F. Morrison (1973), Vector magnetic anomalies derived from measurements of a single component of the field, *Geophysics*, *38*, 359–368, doi:10.1190/1.1440346.

Maloof, A. C., G. P. Halverson, J. L. Kirschvink, D. P. Schrag, B. P. Weiss, and P. F. Hoffmann (2006), Combined paleomagnetic, isotopic, and stratigraphic evidence for true polar wander from the Neoproterozoic Akademikerbreen Group, Svalbard, Norway, *Geol. Soc. Am. Bull.*, *118*, 1099–1124, doi:10.1130/B25892.1.

Marple, S. L. (1987), *Digital Spectral Analysis With Applications*, Prentice-Hall, Englewood Cliffs, N. J.

Mickus, K. L., and J. H. Hinojosa (2001), The complete gravity gradient tensor derived from the vertical component of gravity: A Fourier trans-form technique, *J. Appl. Geophys.*, *46*, 159–174, doi:10.1016/S0926-9851(01)00031-3.

Nelson, J. B. (1986), An alternate derivation of the three-dimensional Hilbert transform relations from first principles, *Geophysics*, *51*, 1014–1015, doi:10.1190/1.1442141.

Nelson, J. B. (1988), Calculation of the magnetic gradient tensor from total field gradient measurements and its application to geophysical interpretation, *Geophysics*, *53*, 957–966, doi:10.1190/1.1442532.

Oppenheim, A. V., A. S. Willsky, and S. Hamid (1996), *Signals and Systems*, 2nd ed., Prentice-Hall, Upper Saddle River, N. J.

Paige, C. C., and M. S. Saunders (1982), LSQR: An algorithm for sparse linear equations and sparse least squares, *Trans. Math. Software*, *8*, 43–71, doi:10.1145/355984.355989.

Pedersen, L. B. (1989), Relations between horizontal and vertical gradients of potential fields, *Geophysics*, *54*, 662–663, doi:10.1190/1.1442694.

Pedersen, L. B., T. M. Rasmussen, and D. Dyrelius (1990), Construction of component maps from aeromagnetic total field anomaly maps, *Geophys. Prospect.*, *38*, 795–804, doi:10.1111/j.1365-2478.1990.tb01875.x.

Purucker, M. E. (1990), The computation of vector magnetic anomalies: A comparison of techniques and errors, *Phys. Earth Planet. Inter.*, *62*, 231–245, doi:10.1016/0031-9201(90)90168-W.

Roth, B. J., N. G. Sepulveda, and J. P. Wikswo Jr. (1989), Using a magnetometer to image a two-dimensional current distribution, *J. Appl. Phys.*, *65*, 361–372, doi:10.1063/1.342549.

Spaggiari, C. V., R. T. Pidgeon, and S. A. Wilde (2007), The Jack Hills greenstone belt, Western Australia Part 2: Lithological relationships and implications for the deposition of ≥4.0 Ga detrital zircons, *Precambrian Res.*, *155*, 261–286, doi:10.1016/j.precamres.2007.02.004.

Tan, S., Y. P. Ma, I. M. Thomas, and J. P. Wikswo (1996), Reconstruction of two-dimensional magnetization and susceptibility distributions from the magnetic field of soft magnetic materials, *IEEE Trans. Magn.*, *32*, 230–234, doi:10.1109/20.477575.

Thomson, B. S., J. B. Bruckner, and A. M. Bruckner (2001), *Elementary Real Analysis*, 1st ed., 735 pp., Prentice-Hall, Upper Saddle River, N. J.

Vestine, E. H., and N. Davids (1945), Analysis and interpretation of geomagnetic anomalies, *Terr. Magn. Atmos. Electr.*, *50*, 1–36, doi:10.1029/TE050i001p00001.

Volk, M., S. Whitlock, C. H. Wolff, B. V. Hall, and A. I. Sidorov (2008), Scanning magnetoresistance microscopy of atom chips, *Rev. Sci. Instrum.*, *79*, 023702, doi:10.1063/1.2839015.

Weiss, B. P., E. A. Lima, L. E. Fong, and F. J. Baudenbacher (2007), Paleomagnetic analysis using SQUID microscopy, *J. Geophys. Res.*, *112*, B09105, doi:10.1029/2007JB004940.

Zauderer, E. (1988), *Partial Differential Equations of Applied Mathematics*, 2nd ed., 891 pp., John Wiley, New York.

————————————

E. A. Lima and B. P. Weiss, Department of Earth, Atmospheric, and Planetary Sciences, Massachusetts Institute of Technology, Cambridge, MA 02139, USA. (limaea@mit.edu)